Biomagnetic characterisation of air pollution particulates in Lahore, Pakistan

Hassan Aftab Sheikh[1,1], Barbara A. Maher[2,2], Vassil Karloukovski[2,2], Giulio Isacco Lampronti[1,1], and Richard Harrison[1,1]

[1]University of Cambridge
[2]Lancaster University

November 30, 2022

Abstract

We report the first characterisation of anthropogenic magnetic particulate matter (MPM) collected on leaves from roadside *Callistemon* trees from Lahore, Pakistan, and on known sources of traffic-related particulates to assess the potential of first-order reversal curve (FORC) diagrams to discriminate between different sources of anthropogenic magnetic particles. Magnetic measurements on leaves indicate the presence of surface-oxidised magnetite spanning the superparamagnetic (< 30 nm) to single-domain (˜30-70 nm) to vortex size range (˜70-700 nm). Fe-bearing particles are present both as discrete particles on the surface of larger mineral dust or carbonaceous particles and embedded within them, such that their aerodynamic sizes may be decoupled from their magnetic grain sizes. FORC diagrams of brake-pad residue specimens show a distinct combination of narrow central ridge, extending from 0-200 mT, and a low-coercivity, vertically spread signal, attributed to vortex and multi-vortex behaviour of metallic Fe. This is in agreement with scanning electron microscopy results that show the presence of metallic as well as oxidised Fe. Exhaust-pipe residue samples display a more conventional 'magnetite-like' signal comprising a lower coercivity central ridge (0-80 mT) and a tri-lobate signal attributed to vortex state and/or magnetostatic interactions. The FORC signatures of leaf samples combine aspects of both exhaust residue and brake-pad endmembers, suggesting that FORC fingerprints have the potential to identify and quantify the relative contributions from exhaust and non-exhaust (brake-wear) emissions. Such measurements may provide a cost-effective way to monitor the changing balance of future particulate emissions as the vehicle fleet is electrified over the coming years.

Biomagnetic characterisation of air pollution particulates in Lahore, Pakistan

[1]H.A. Sheikh, [2]B.A. Maher, [2]V., Karloukovski, [1]G.I. Lampronti,[1]R. J. Harrison

[1]1Department of Earth Sciences, Downing Site, Cambridge, CB2 3EQ
[2]Centre for Environmental Magnetism and Palaeomagnetism, Lancaster Environment Centre, University of Lancaster, Lancaster, LA1 4YB, U.K.

Key Points:

- Microscopy and magnetic measurements of tree leaves indicate different sources of anthropogenic particulate air pollution.
- First-order reversal curves (FORCs) can potentially be used as a proxy to identify particulate sources
- High concentrations of Fe-bearing ultra-fine particles found in brake-pad and exhaust-pipe residue specimens.

Corresponding author: Hassan Aftab Sheikh, has57@cam.ac.uk

Abstract

We report the first characterisation of anthropogenic magnetic particulate matter (MPM) collected on leaves from roadside Callistemon trees from Lahore, Pakistan, and on known sources of traffic-related particulates to assess the potential of first-order reversal curve (FORC) diagrams to discriminate between different sources of anthropogenic magnetic particles. Magnetic measurements on leaves indicate the presence of surface-oxidised magnetite spanning the superparamagnetic ($<$ 30 nm) to single-domain (30-70 nm) to vortex size range (70-700 nm). Fe-bearing particles are present both as discrete particles on the surface of larger mineral dust or carbonaceous particles and embedded within them, such that their aerodynamic sizes may be decoupled from their magnetic grain sizes. FORC diagrams of brake-pad residue specimens show a distinct combination of narrow central ridge, extending from 0-200 mT, and a low-coercivity, vertically spread signal, attributed to vortex and multi-vortex behaviour of metallic Fe. This is in agreement with scanning electron microscopy results that show the presence of metallic as well as oxidised Fe. Exhaust-pipe residue samples display a more conventional 'magnetite-like' signal comprising a lower coercivity central ridge (0-80 mT) and a tri-lobate signal attributed to vortex state and/or magnetostatic interactions. The FORC signatures of leaf samples combine aspects of both exhaust residue and brake-pad endmembers, suggesting that FORC fingerprints have the potential to identify and quantify the relative contributions from exhaust and non-exhaust (brake-wear) emissions. Such measurements may provide a cost-effective way to monitor the changing balance of future particulate emissions as the vehicle fleet is electrified over the coming years.

1 Introduction

Epidemiological studies have associated particulate air pollution with reduced cognitive performance (Zhang et al., 2018), development of diseases in the pulmonary and cardiovascular systems (Schwarze et. al, 2006) and dementia (Chen et al., 2017). The biological mechanisms behind higher risk of cardio-respiratory diseases in an air-polluted urban environment have been studied and associated with ultrafine particles (Penttinen et al., 2001; Leitte et al., 2013; Miller et al., 2017). The size, morphology and chemical composition of particles are critical in gauging detrimental effects to human health. Conventional air pollution indices classify and monitor PM as a function of its aerodynamic diameter; Exposure to $PM_{0.1}$ (0.1 µm), often referred to as ultrafine particles (UFPs), is of increasing focus and concern because of their potential adverse health implications, as small particles can exert higher toxicity than larger particles (Ohlwein et al., 2019). UFPs can be drawn into the body via ingestion(Calderón-Garcidueñas et al, 2020), skin (Araviiskaia et al., 2019), olfactory transport and through the lungs, entering the alveoli and penetrating biological membranes, effectively translocating to almost all organs (Ohlwein et al. 2019; Schraufnagel, 2020). UFPs have been linked to cardiovascular, Alzheimer's disease, neurological, and chronic respiratory diseases (Maher et al., 2020, Maher et al., 2019, Calderón-Garcidueñas et al., 2019, Devlin, 2014; Calderón-Garcidueñas et al. 2016; Rückerl et al. 2011). Particulates containing traces of heavy metals such as Zn, Cr, Mn, Fe, Cu, and Pb have adverse effects on human lung epithelial cells because of their high toxicity and their complex interactions with other metal contaminants (Yuan Y et al., 2019). Fe-bearing UFPs have been linked to respiratory diseases (Dusseldorp et al., 1995), mitochondrial dysfunction (Maher et al., 2020) and have also been found in human brain, where they may play a role, via the Fenton reaction, in the development of neurodegenerative diseases (Maher et al., 2016). The serious potential health impacts of Fe-bearing UFPs makes the use of magnetic measurements to characterise and monitor airborne particles a particularly powerful tool. Particle magnetic properties change fundamentally over the size range of nanometres to PM_{10}, and can be used to discriminate effectively between different magnetic phases. Therefore, both room-temperature and low-temperature magnetic measurements have great potential for discriminating between sources of PM. Moreover, by resolving different Fe minerals and their oxidation states (Fe^0 vs Fe^{2+} vs

Fe^{3+}), the toxicity potential of Fe-bearing nanoparticles and their human health impacts can be determined (Gonet and Maher, 2019). Biomonitoring studies have correlated magnetic properties with PM10 and PM2.5 concentrations (Matzka and Maher, 1999; Muxworthy et al., 2001; Hofman et., 2014), transition and heavy metals such as Co, Sr, Zn, Ni, Pb, Ti (Spassov et al., 2004; Maher et al., 2008; Hofman et al., 2020) and polycyclic aromatic hydrocarbons (PAHs) (Lehndorff and Schwark, 2004). A particle's size, surface area, and solubility are major determinants of its toxicity. Iron oxides and hydroxides are effective sorbents of heavy metals because of their large surface area (Cornell and Schwertmann 1996). The toxicity potential of metals derived from traffic-related sources (exhaust and non-exhaust) has also been linked with the presence of endotoxins which can sit on particle surfaces, and exacerbate the production of reactive oxygen species (ROS), leading to chronic health implications (Kelly and Fussell, 2012). Recent roadside (Gonet et al., 2021a) and airborne brake wear (Gonet et al., 2021b) characterisation studies show that the contribution of Fe-rich particles from brake-wear emissions is very high compared to other particulate sources in urban macroenvironments, and that more than 99% of brake wear particles are <200 nm. Therefore, a focus on Fe-bearing UFP is timely, and the use of magnetic properties as a tool for determining different sources of particulates is our primary goal.

Air quality in Lahore, Pakistan is one of the worst in the world, reaching unhealthy levels on most days according to the Air Quality Index (AQI) - which is based on the measurement of $PM_{2.5}$ and PM_{10} mass concentrations, as well as other major pollutants (ground level ozone, CO, NO_2, SO_2). However, these real-time but spatially restricted, mass-based measurements are unlikely to capture fully the adverse health risks posed specifically by Fe- and other co-associated metal-bearing UFPs. In this study, we aim to provide a morphological, chemical, and magnetic characterisation of airborne particulate matter in Lahore and then apply magnetic approaches to identify and characterise Fe-particles and their sources. The lack of a standardised method to monitor these particles means that these can go undetected. We report the distinctive magnetic fingerprints of different PM sources (exhaust and non-exhaust emissions) and discuss the extent to which these can be detected and quantified using a biological proxy (leaves, in our study).

2 Materials and Methods

2.1 Sampling Campaign

Figure 1 (A) Location of area of study and the nearby industrial estates and brick kilns. (B) Area of study showing the sampled trees and their distance from Canal bank road and the service lane.

The study site is located next to a heavy-trafficked residential and commercial area of Canal Road, Lahore (Fig. 1A). It consists of four-opposing lanes and is separated by a canal, lined by different species of trees. The chosen sampling site was a 22 m wide green-belt adjacent to the west-bound carriageway, consisting of bottlebrush trees (Callistemon), an evergreen species, chosen because of its abundance in the vicinity (Fig. 1A) and hair-like features on its leaf surface. The site was first visited on 10th February 2021 in order to mark the leaves which had started to grow approximately 10 days prior to the site visit. A mixture of both freshly grown leaves (estimated exposure time of 20-26 days) and leaves which had been exposed for approximately one year were collected. The height of tree crowns varied but as we are interested in exposure at inhalation height, we sampled at 1.5 m (which coincided with the base of the crown). Ten tree crowns were sampled by carefully picking leaves from the petiole during the period 17th - 26th February 2021; there was no rainfall recorded since the fresh leaves started growing. From each tree, we collected leaves facing away from and towards the road. From our trees of interest, 30 leaves were analysed (lower than the expected 60 samples either because of absence of fresh leaves in some tree crowns or because some leaves were discarded by the Plant Health Protection Department). The leaves were kept in plastic bags and refrigerated before magnetic and microscopic analysis. After initial magnetic analysis, the leaves were oven dried at 40 °C for two days and powdered for low-temperature magnetic measurements and x-ray diffraction (XRD). To characterise the particulates on leaves in terms of exhaust vs non-exhaust contribution, we collected residue samples from petrol exhaust pipes, diesel exhaust pipes and brake pads of different vehicles in Lahore (Table S16, supplement). These were obtained by scraping an A4 sheet of paper on the inside of exhaust

pipes and brake pads of cars, vans, and rickshaws. Microscopy and magnetic analysis were carried out on these residue samples on the paper to evaluate their contribution to the particles observed and measured for the leaves.

2.2 Microscopy and chemical analysis

We performed backscattered electron (BSE) and secondary electron (SE) imaging and chemical characterisation, using energy dispersive X-ray spectroscopy (EDX), of PM present in our leaves using a Thermofisher Quanta-650F scanning electron microscope (SEM) (nanometre resolution with magnification range 5-1,000,000 x) equipped with two Bruker XFlash 6|30 EDS detectors at the Department of Earth Sciences, University of Cambridge. Leaf specimens were carbon coated to prevent charging. Imaging was performed under high vacuum at both low accelerating voltages (2-5 kV) and high accelerating voltages (15 kV) using a spot size of 3.5-4.5. For microanalysis of ferro or ferrimagnetic minerals, we used 15 kV specifically to obtain the K-line excitation for Fe. This was performed to evaluate the morphology and chemistry of Fe-bearing minerals present and evaluate the association of magnetic carriers with other particulates.

2.3 X-ray diffraction

XRD measurements on powdered leaf specimens were performed in Bragg-Brentano geometry on a D8 Bruker diffractometer equipped with a Mo K primary beam operating at 50 kV and 40 mA and a LYNXEYE XE-T position sensitive detector. Collection conditions: 2-30° 2 range, 0.025° step size, 3 seconds/step, divergence slits 0.2.

2.4 Magnetic analysis

The PM-laden leaves were analysed for their bulk magnetic properties at the Centre for Environment Magnetism and Paleomagnetism (CEMP), Lancaster University. The surface area (m2) of the leaves was determined, using a scanner, to normalise our results; the samples were wrapped in cling film and firmly pushed into 7 cm^3 polycarbonate pots for magnetic analysis. A Molspin demagnetiser (with DC attachment) was used to impart an anhysteric remanent magnetisation (ARM) at 80 milliTesla (mT) alternating current (AC) field and 100 T direct current (DC) bias field ($ARM_{80/100}$). Dividing ARM by the DC bias field yields the ARM susceptibility (χ_{ARM}). The samples were subsequently alternating field (AF) demagnetised at 10 mT, 15 mT, 20 mT, 25 mT and 30 mT. A second set of measurements included acquisition of room-temperature isothermal remanent magnetisation (IRM) at 20 mT, 100 mT using a Molspin pulse magnetizer; 300 mT and 1T) was acquired using a Newport electromagnet. The high-field remanent magnetisation (HIRM) was used to calculate the relative contribution of hematite using the ratio (IRM_{1000}-IRM_{300})/$SIRM_{1000mT}$, which assumes that all the IRM acquired between 300-1000 mT is proportional to the amount of hematite present (Maher et al., 1999). All remanence measurements were made at high speed of rotation on an AGICO JR-6A magnetometer (sensitivity 2.4 x 10^{-6} Am^{-1}) with a metal shield option to create true zero field.

To help identify which magnetic phases are present on the leaf samples, we conducted low-temperature measurements on a Quantum Design Magnetic Property Measurement System (MPMS) at the Maxwell Centre, University of Cambridge. Measurements were conducted on two leaf samples, two brake-pad samples and two exhaust-pipe samples according to the following sequence: 1) a room-temperature SIRM (RT-SIRM) was imparted in a 2.5 T field and then measured on cooling from 300 K to 10 K; 2) the RT-SIRM was then measured on warming back to 300 K; 3) the sample was zero-field cooled (ZFC) to 10 K and a low-temperature SIRM (LT-SIRM) imparted in a 2.5 T field; 4) the ZFC LT-SIRM was measured on warming to 300 K; 5) the sample was then field cooled (FC) in 2.5 T from 300 to 10 K and the resulting FC LT-SIRM was measured from

10 K to 300 K. The instrument did not have a low-field cancellation option, and residual fields can range from 0.5-20 mT depending on the sequence used. Although the presence of a residual field complicates the interpretation of the curves (in particular, 'ZFC' may not strictly be zero-field cooling and all 'remanence' measurements may have an additional induced component of magnetisation), the data are sufficient to achieve the primary goal of detecting the presence of a Verwey transition and the rapid loss of LT-SIRM on warming that may be associated with superparamagnetic (SP) particles.

Hysteresis parameters, DC demagnetisation curves and first-order reversal curves (FORCs) were measured at room temperature using a Princeton Measurement Corporation MicroMag Accelerating Gradient Magnetometer (AGM) at the Nanopaleomagnetism Lab, University of Cambridge. Leaves, brake pad and vehicle exhaust pipe residue samples were cut into 4x4 mm squares and mounted on the probe using grease. Due to the weak nature of the signals being measured, extra care was taken to account for any potential contamination of the AGM sample probe. A blank, greased probe measurement was taken before every hysteresis measurement to account for any remanence contribution from the probe; this blank measurement was averaged and subtracted from measured hysteresis loops. Multiple FORCs were acquired and averaged twice for each sample at 1 mT field step and an averaging time of 300 ms in discrete mode. FORC diagrams were processed using the VARIFORC algorithm (Egli, 2013) within the FORCinel software of Harrison and Feinberg (2008), with variable smoothing factors that are given in respective diagrams.

3 Results

3.1 Chemical, crystallographic, and morphological classification of leaf PM

The majority of the leaf-deposited PM we observed is 'non-magnetic', with variably geogenic, biogenic or anthropogenic origins. We identified a total of nine particle types: mineral dust, carbonaceous particles, heavy metals, fly ash, soot, Ca-sulfate, secondary aerosol particles, biogenic particles (pollen), and Fe-bearing particles (Table S19; Fig. 2). These particles were classified based on their elemental composition using the EDX spectra and their morphology. To get a representative set of data, we looked at BSE images and EDX maps of leaf specimen T10-1Y-TSL (because it was exposed for an entire growing season) at four different horizontal field width (HFW) ranges – 100 µm, 30 µm, 10 µm, and 2 µm. For the size-focused classification of PM, 1482 particles were analysed and binned into different size ranges of >2.5 µm, 1.0-2.5 µm, and <1.0 µm (Fig. S1, supplement).

Mineral dust particles (e.g., Fig. 2D, 2H) were the most abundant particles in the >2.5 µm leaf fraction. These particles were mostly irregular, sometimes agglomerated with other particles, and contained primarily Si, Al, Ca along with other associated elements, Fe, Mn, Mg, K and F. Chemical phases recognised from EDX were Al-silicate (Fig. 2A), Ca-Al silicate (Fig. 2H), and XRD identified whewellite, anorthite (Ca-feldspar) and anhydrite [which could be both naturally occurring and/or anthropogenic] (Fig. S14, supplement).

Carbonaceous particles tended to display a range of morphologies, from spherical (Fig. 2H) to irregular (Fig. 2B). It was possible to distinguish anthropogenic carbonaceous particles from pollen grains based on their morphological features and sometimes from the presence of minor traces of K in the biomass burning-derived carbonaceous particles.

Heavy metals such as Zn (Fig. S2, supplement), Ba (Fig. S3, supplement) and metal oxides such as Ti-oxide (Fig. S4, supplement) were observed in the SEM/EDX analy-

sis. The particle sizes of metal-bearing particles ranged from 500 nm to 2.5 µm; they occurred both as discrete particles and in association with Fe-oxides or silicates.

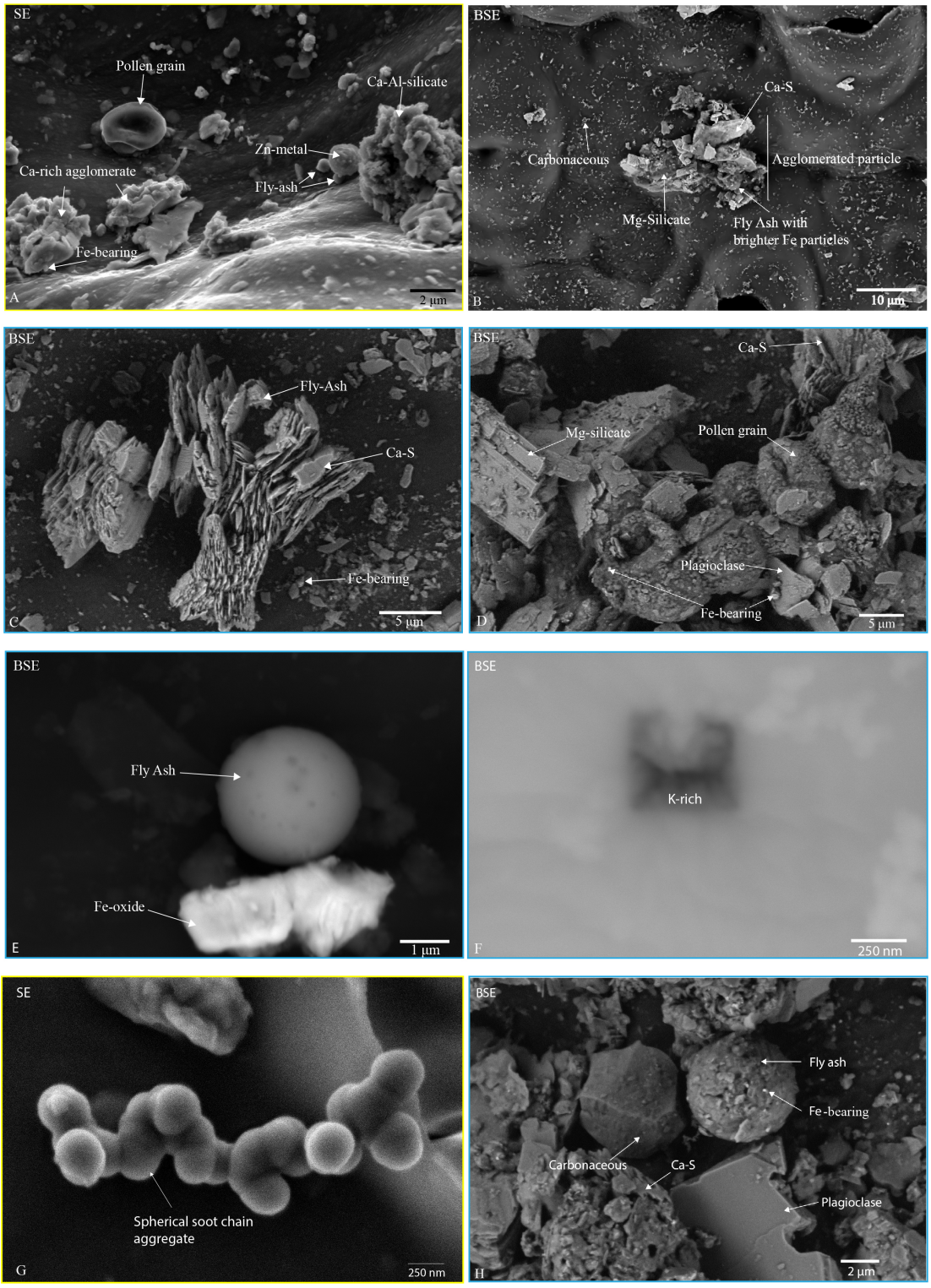

Figure 2 SEM images of adaxial side of leaves. (A) Secondary electron (SE) image of fly ash particles clustered with Zn-rich spherical particle and Fe-bearing particle associated with Ca-sulfate agglomerate. (B) BSE image of a calcium-sulfate agglomer-

ate clustered together with fly ash having many Fe-bearing ultrafine particles on its surface. (C) Smooth platy-like gypsum particle. (D) Spherical pollen grains. (E) Smooth spherical fly ash particle. (F) K-rich rectangular particle. (G) Chain-like aggregate of soot particles. (H) Rectangular plagioclase, and a spherical carbonaceous particle. (Blue border: BSE, Yellow border: SE)

Fly ash particles had a characteristic smooth, spherical morphology, with size range usually between 1–2 µm. They contained primarily Si, Al, O and were sometimes coated with aggregates of finer particles containing Fe, Mn, Mg and Ca. (Fig 2E).

Soot particles had a distinct chain-like morphology (Fig. 2G) and were composed primarily of C spheres, typically 200 nm in diameter or smaller. K-rich aerosol particles we observed were irregular-rectangular shaped, 0.5-2 µm in size, and were often coated with organic carbon (Fig. 2F) or associated with soot (Fig. S6, supplement).

Calcium sulfate (CaSO4) particles (Fig. 2C) were abundant and dominantly on the coarser end of the size spectrum (>2.5 µm) with a distinctive morphology of stacked, cleaved platelets.

Biogenic particles, such as pollen (Figs. 2A, 2D), were classified separately from other carbonaceous particles. Pollen grains had a spherical-elliptical morphology and were dominantly coarser (>2.5 µm) with high C and O content. Whewellite (Fig. S4, supplement) was also recognised as a biogenic particle, displaying euhedral particles in the size range 1-2 µm.

Fe-bearing particles on the leaf surfaces were present both as discrete particles and on the surface of (or embedded within) other metal- or non-metal-bearing particles (Fig. 3). The diameter of Fe-bearing particles varied between <0.1- 2.5 µm, with most particles ranging from <0.1-1.0 µm. In some cases, Fe-bearing particles were clustered together and sometimes associated with soot particles (Fig. S5, supplement); BSE imaging showed that some ultrafine Fe-rich particles were embedded within silicates (Fig. 3C).

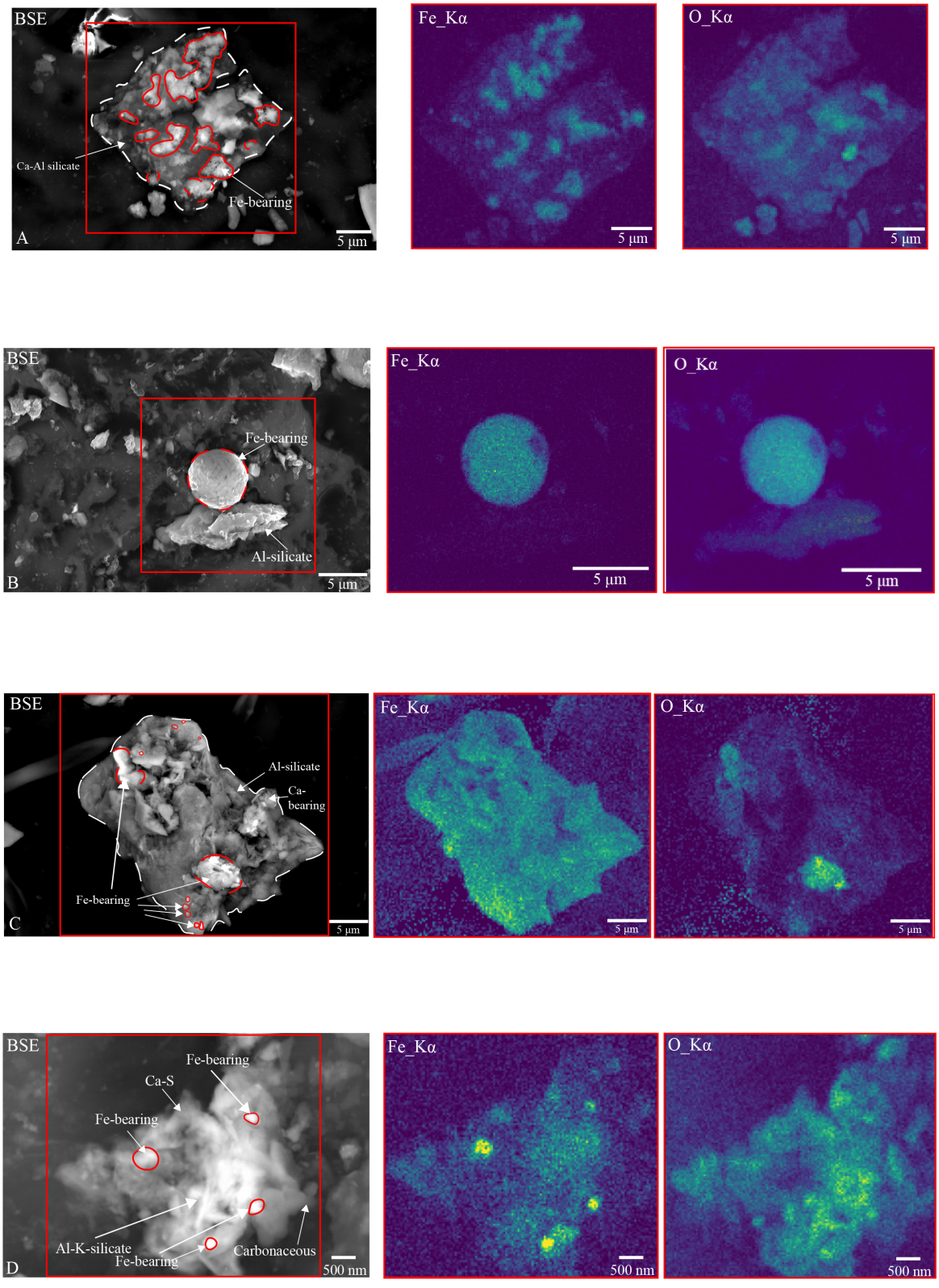

Figure3 SEM images and EDX maps of Fe-bearing particles. (A) Cluster of Fe metal particles, ranging from 2.5 µm to less than 1 µm, embedded on surface of an Al-silicate; they exhibit a spiky ball morphology. (B) A spherical Fe-oxide particle (possibly from high temperature combustion reaction sitting on top of an Al-silicate. (C) Clusters of

micron-sized Fe particles and a few discrete nanoparticles appear to be physically enclosed within a silicate particle. (D) Nano-sized Fe-bearing particles embedded within a silicate and carbonaceous agglomerate. [All images are BSE]

Discrete Fe particles, usually in the range of 0.1-1.0 µm, were rounded-subspherical, while some of the spherical Fe-bearing particles had a dendritic-like texture and looked very similar to fly ash particles (Fig. 3B). Fe particles were present both on the adaxial (upper) and abaxial (lower) side of the leaves, with a higher concentration on the adaxial side. EDX analysis showed all observed Fe-bearing particles were oxidised; in accord with our magnetic analysis (see section 3.4) which confirmed the presence of surface oxidised magnetite with a small contribution from a higher coercivity phase (potentially hematite).

XRD patterns (Fig. S14 A-D, supplement) for leaf sample (T1-AW-1Y) showed three major phases in the following abundance order: whewellite (calcium oxalate) (Fig. S5, supplement), anorthite (Ca-feldspar), and anhydrite. Calcium oxalate ($CaC_2O_4{\cdot}(H2O)_x$) is a biomineral and can form in leaves as a way to regulate calcium levels in plant tissues and organs (Franceschi, 2001) by re-precipitating solubilised calcium (Glasauer et al., 2013). No Fe-oxide or Fe-metal peaks were observed.

3.2 Particles from exhaust and non-exhaust specimens

SEM/EDX analysis was conducted on residue particles collected from a Toyota Corolla XLI brake pad, Suzuki Alto brake pad, XLI petrol exhaust and Mazda truck 3.5 L diesel exhaust pipe (Fig. 4). The brake-pad specimen from a Toyota XLI showed abundant metallic Fe and Fe-bearing particles (Fig. 4A). The particle sizes ranged from sub-micrometre to $>$ 2 m. The EDX spectra of Fe-bearing particle (2) show an Fe-oxide within a silicate phase. Petrol exhaust-pipe residue samples (Fig. 4B) show the presence of irregular Fe-bearing particles ranging in size from 0.5-3 m; EDX analysis of particle (3) shows a subhedral silicate particle enriched in Fe. EDX also identified the abundance of calcium-rich particles but also other anthropogenic metals such as Cr (Fig. 4B). EDX for the Mazda truck 3.5 L diesel exhaust pipe particles showed the presence of finer Fe-bearing particles ($<$2.5 m) within sulfur-rich carbonaceous particles ($>$2.5 m) (Fig. 4C). Heavy metals such as Mn, Al, and Cr of size ranges around 1- 4 m were also observed to be associated with Fe-bearing particles (Fig. S11 and S12, supplement) in the XLI petrol exhaust specimen. The soot nanospheres observed on the leaves (Fig. 2G) were also observed in the diesel exhaust pipe specimen (Fig. S13, supplement) and were associated with Ca.

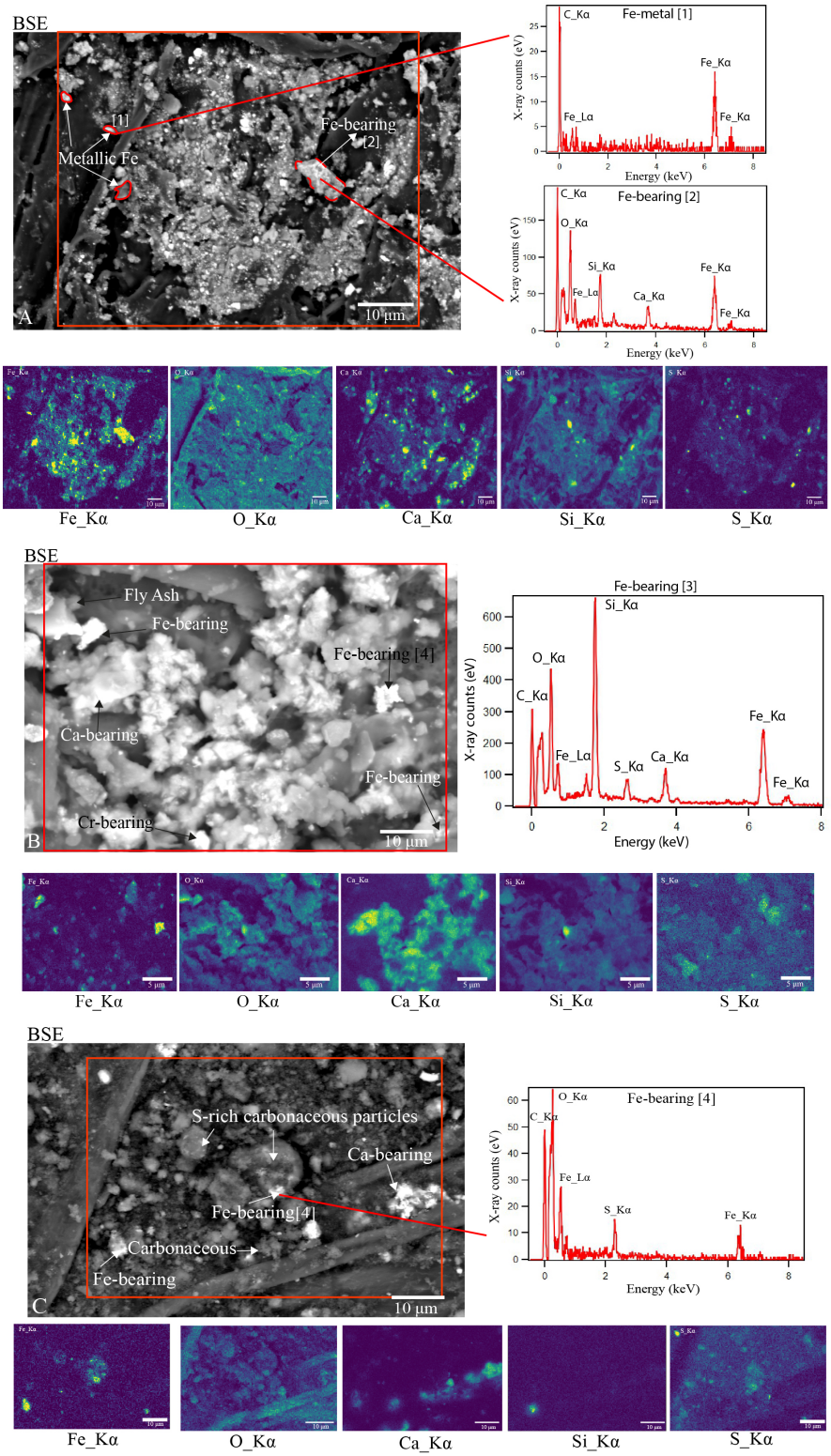

Figure 4 (A) Brake pad samples of XLI, showing nano-sized Fe-metal particles within silicate. EDX spectra for particles [1] shows the presence of metallic Fe and [2] oxidised Fe. **(B)** XLI petrol exhaust showing irregular morphology of Fe particles; EDX spectra of particle [3] shows Fe-bearing particle embedded on top of a silicate **(C)** BSE image of Mazda truck 3.5 L diesel exhaust pipe showing nano-sized Fe-particles embed-

ded on top of a silicate mineral and the corresponding EDX map [4] shows the presence of sulfur with Fe-bearing particles.

3.3 Leaf SIRM variation

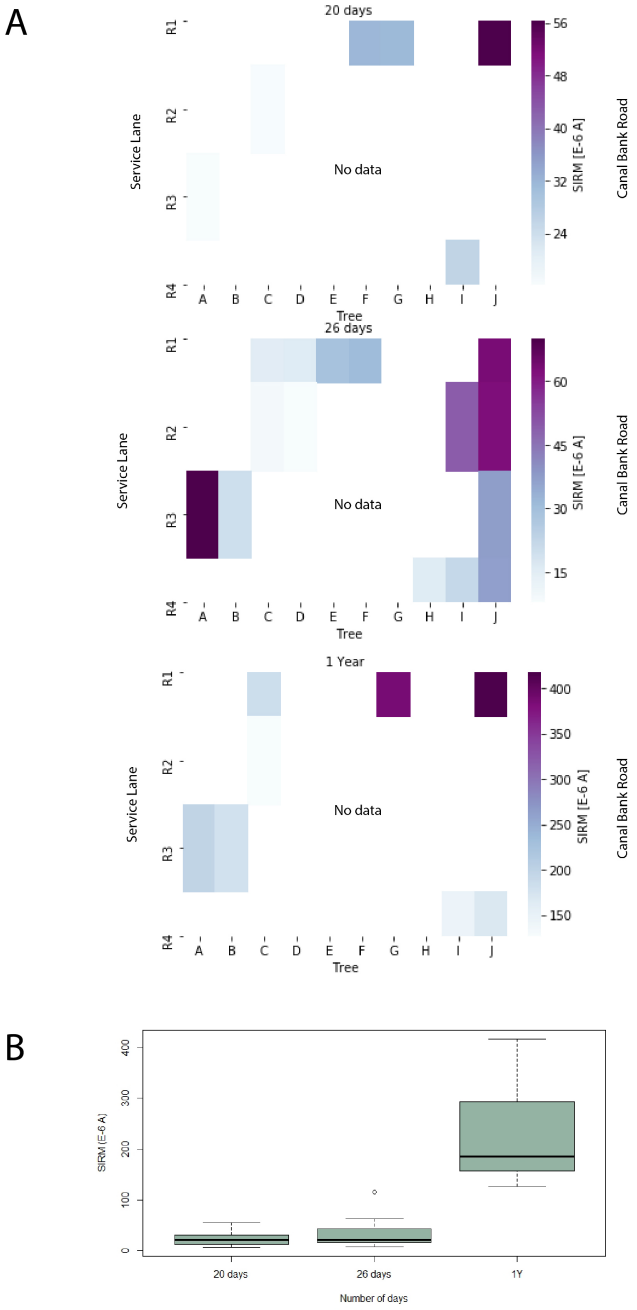

Figure 5 (A) Temporal and Spatial variation on measured leaf specimens (see Fig. 1B for Tree positions). **(B)** shows the average SIRM values of leaf specimens over different timescales

Both temporal and spatial variations in surface area specific SIRM were observed in tree crowns along the green belt (Fig. 5). Leaf SIRM values increased with longer exposure time (Fig. 5B) and are consistent with similar studies conducted previously (Table S18, supplement; Muxworthy et al., 2002; Kardel et al., 2011; Mitchell et al., 2009;

Hofman et al., 2015). The higher magnetic signals were from samples collected closer to the main canal bank road or the service lane (Fig. 5A) and exposed for the longest (1 year). T1, facing towards the road, had a maximum SIRM value of 417.9 x 10^{-6} A. This was 7.5 times higher than a leaf exposed for 20 days and facing away from the road (56.2 x 10^{-6} A) (Fig. 5B). HIRM% of all our specimens was between 2.5-6%, suggesting some contribution from a high-coercivity magnetic component.

3.4 Low-temperature magnetic properties

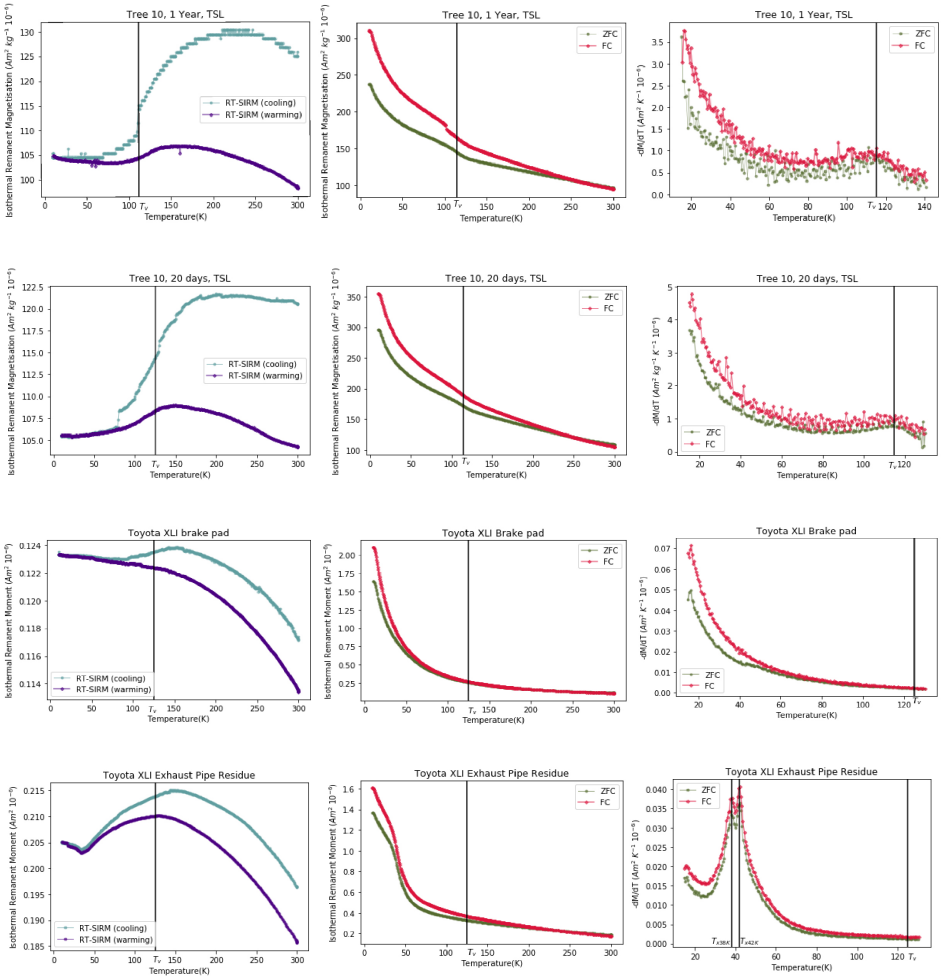

Figure 6 A 2.5 T field was applied to our samples to get room-temperature saturation isothermal magnetic remanence (RT-SIRM). The samples were then cycled from 300 K to 10 K and back to 300 K in zero-field, giving us two curves: RT-SIRM (cooling- 300- 10 K) and RT-SIRM (warming – 10 K to 300K). ZFC-FC warming curves where IRM for FC was acquired at 2.5 T at 10 K. ZFC-FC curves show a peak at Verwey transition for leaf specimens at 115 K. RT SIRM cooling curve for XLI exhaust shows a peak at around 32 K, possible hint at pyrrhotite. Leaf specimens T10-1Y-TSL and T10-20d-TSL are mass normalised by dry weigh of leaf powder measured using the gel cap; an accurate mass normalisation was not possible for brake and exhaust-pipe specimens; therefore, absolute moment values are reported for them. Values for -dM/dT vs temperature graph were taken from 12 K instead of 10 K because the temperature was not stabilised at low temperatures, hence contributing to slight curvature in -dM/dT at 10-12 K.

RT-SIRM and ZFC/FC LT-SIRM curves of powdered leaf specimens exposed for 1 year (T10-TSL-1Y) and 20 days (T10-TSL-20d) were measured and mass-normalised

to see if there is any temporal variation in magnetic properties. Both specimens show a dampened Verwey transition at a temperature of around 115 K (Fig. 6A and 6B, Table 1B). There is a weak but distinct partial recovery of remanence during warming back through the Verwey transition. The temperature-derivative of LT-SIRM curves of leaf specimens shows that remanence decreases swiftly from 10-60 K, more slowly from 60-100 K, followed by an acceleration of remanence loss at the Verwey transition. Both samples have FC > ZFC remanence, with the difference between FC and ZFC persisting to a temperature of 250 K.

RT-SIRM and ZFC/FC LT-SIRM curves of the XLI-brake-pad specimen are quite different to those of the leaf samples. Peak RT-SIRM occurs at 150 K rather than 200 K and shows a smaller remanence loss of 0.63% (at 50 K) on cooling through the Verwey transition (Table 1A). The temperature-derivative of LT-SIRM curves shows that remanence decreases swiftly from 10-60 K and more slowly from 60-300 K. FC vs ZFC difference is less pronounced than that for leaf specimens and there is no discernible difference for temperatures above 100 K. RT-SIRM and ZFC/FC LT-SIRM curves of the exhaust-pipe specimen are distinct from both leaf and brake-pad samples. A distinct kink in RT-SIRM at 32 K is observed, which is reversible on warming. There is no distinct recovery of remanence associated with warming back through the Verwey transition, although the broad hump is largely reproduced. LT-SIRM curves show rapid acceleration of remanence loss from 30 to 60 K, with two distinct peaks in the derivative of both FC and ZFC curves observed at 38 K and 42 K. There is no visible acceleration of remanence loss at the Verwey transition. FC > ZFC remanence, with the difference persisting to at 240 K.

A relative estimate of the superparamagnetic (SP) contribution in our specimens was calculated by comparing the ZFC LT-SIRM at 10 K to the RT-SIRM at 10 K. This measure provides an estimate of particles which are not capable of holding remanence when magnetised at room temperature (unblocked SP) but are able to hold a remanence when cooled to 10 K (blocked SP). Generally, the SP fraction in XLI brake pad and exhaust pipe specimens is higher than in the 1 year and 20-day leaf specimens (Table 1B). For 1 year and 20 days leaf specimens, the RT- SIRM at 10 K represents 44% and 42% of LT-SIRM at 10 K, respectively. For the brake-pad and exhaust specimens, however, the RT-SIRM at 10 K represents just 7% and 13% of the LT-SIRM at 10 K, respectively, meaning that the remaining 93% and 87% of LT-SIRM remanence is carried by particles that were SP at 300 K and become blocked when cooled between 300 and 10 K.

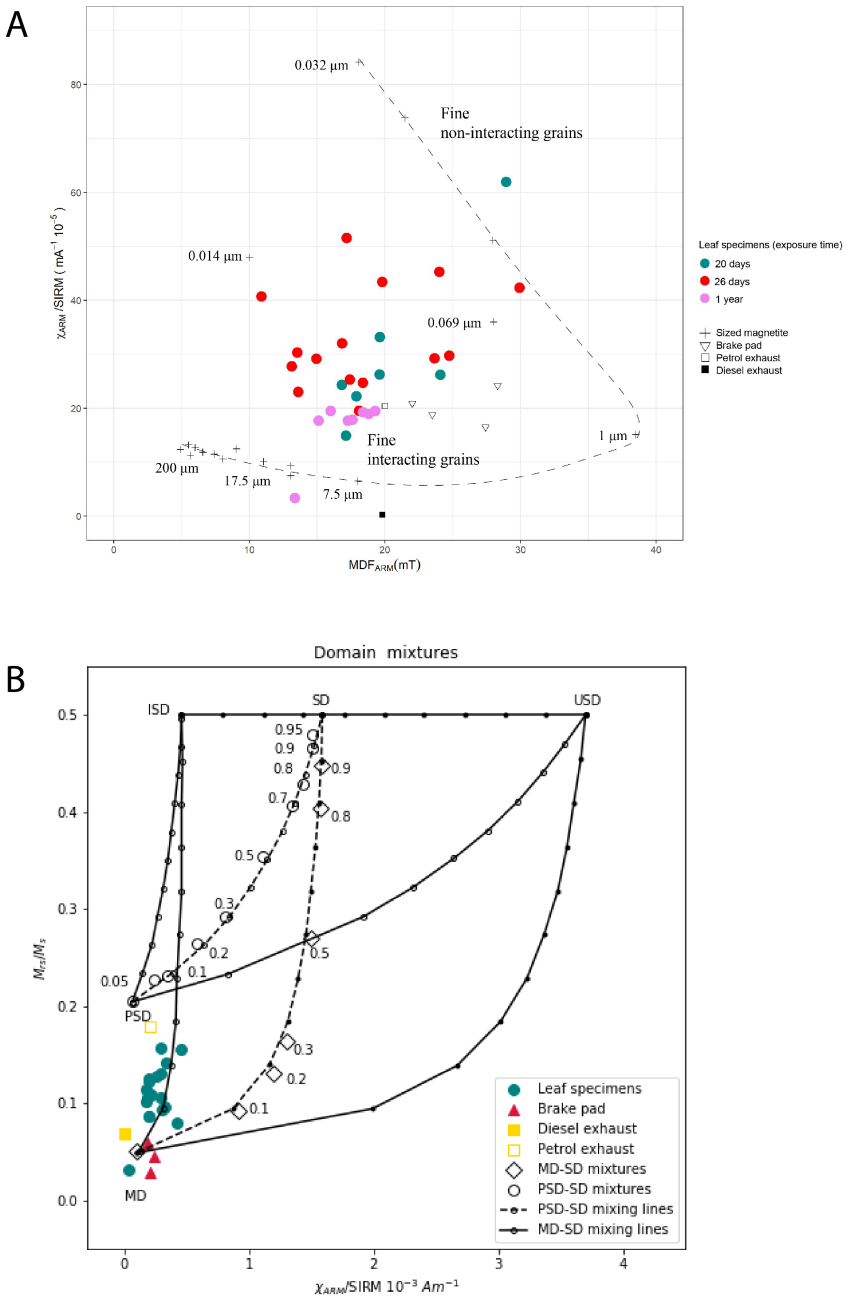

Figure 7 A) shows a comparison of leaf, brake pad and exhaust pipe specimens with sized magnetite grains (Maher, 1988; Dankers, 1978; Özdemir and Banerjee, 1982). This is represented by room temperature ARM susceptibility normalised by saturation isothermal remanent magnetisation (SIRM) vs the ARM mean destructive field (MDF_{ARM}) of each sample, which is defined when the magnetic fraction loses half of its remanent magnetisation. It is indicative of the complicated relationship of mean grain size, where MDF_{ARM} increases with decrease in grain size. B) Leaf, exhaust and non-exhaust specimens are plotted on the M_{rs}/M_s versus χ_{ARM}/M_{rs} for MD-SD (diamonds) and PSD-SD (circles) mixtures (Lascu et al., 2010). The numbers next to the symbols represent SD fraction in the total mixture.

3.5 Magnetic granulometry

Assuming magnetite as the dominant ferrimagnetic component present, the room-temperature ARM/SIRM vs MDF_{ARM} plot (Maher and Taylor, 1988; Maher et. al., 2016) (Fig. 7A) shows that the specimens display a range of magnetite sizes, defining a loose trend bounded by single-domain (SD) grains (32-64 nm) at the fine end and multi-domain (MD) grains (7.5-17 µm) at the coarse end. The majority of our leaf specimens lie within the field of interacting fine-sized magnetite grains. The old (1 year) vs the fresh (20 and 26 days) leaf particles group within the interacting magnetite grains region. Petrol exhaust pipe and brake pad samples also lie within the fine, interacting magnetite region whereas the diesel exhaust pipe falls in a coarser region. Fig. 7B shows our specimen data plotted on the Lascu plot (Lascu et. al, 2010). Our leaf specimens and diesel exhaust pipe specimen lie on the interacting single-domain (ISD) to multi-domain (MD) mixing line, in agreement with Fig. 7A. The brake-pad abrasion residue specimens fall in the MD range. The petrol-exhaust pipe sample falls close to the 'pseudo-single-domain' (PSD), also known as vortex (V) range.

Hysteresis properties of leaves and exhaust and non-exhaust sources were measured at room temperature and averaged over five times to reduce noise and drift. Parameters measured included saturation magnetisation (M_s), saturation remanent magnetisation (M_{rs}), and coercivity (B_c). DC-demagnetisation curves were also measured at room-temperature to obtain the remanent coercivity (B_{cr}). All leaf samples showed narrow hysteresis curves with coercivities (B_{cr}) ranging from 2-15 mT (Fig. S7 and Table S17, Supplement). Specimens exposed for 20 and 26 days were weak and noisy but had similar hysteresis loop shape parameters to the samples exposed for around a year, suggesting sources and resulting leaf magnetic mineralogy were similar (Fig. S8A and S8B, supplement). Brake-pad specimens showed lower bulk coercivities (1.8 mT- 8.2 mT) compared to exhaust-derived specimens. Petrol exhaust pipe specimens had an average coercivity of 9.5 mT, and diesel exhaust pipe had average coercivity of 6.5 mT (Fig. S8, supplement). We measured FORCs for all our specimens at the same parameters of 1 mT field step, 1 T saturation field, an averaging time of 300 ms: repeating the measurement twice to average FORCs. Leaf-specimen FORCs (Fig. 8D) contain both low-coercivity (LC) and high-coercivity (HC) ridge signals, particles that are either strongly interacting (Int) or in V states, and some contribution from SP grains. Less exposed leaves (in terms of both time and spatial positioning from traffic-related source) had lower magnetisable contribution and thus produced significantly noisier data, but near identical patterns of FORC distribution. The Alto brake-pad sample (Fig. 8E) displays a high-coercivity ridge with SP contribution, and vertical spreading along the Bu axis, suggesting an MD signal. Exhaust-pipe signals were dominated primarily by a signal extending modestly along the horizontal B_c axis and some vertical spreading around the SP-SD ridge indicating the presence of Int and/or V states. Backfield IRM distributions (-$dM/dlog(B_c)$) were plotted against $log(B_c)$ (Fig. 8 A-C). The backfield coercivity distributions, extracted directly from the corresponding FORC data, showed that the brake pads are uniformly associated with the highest coercivity component (blue), the exhaust pipe samples with the lowest coercivity contribution (red), and that the leaves (black) have variable coercivity contributions that lie between these two extremes.

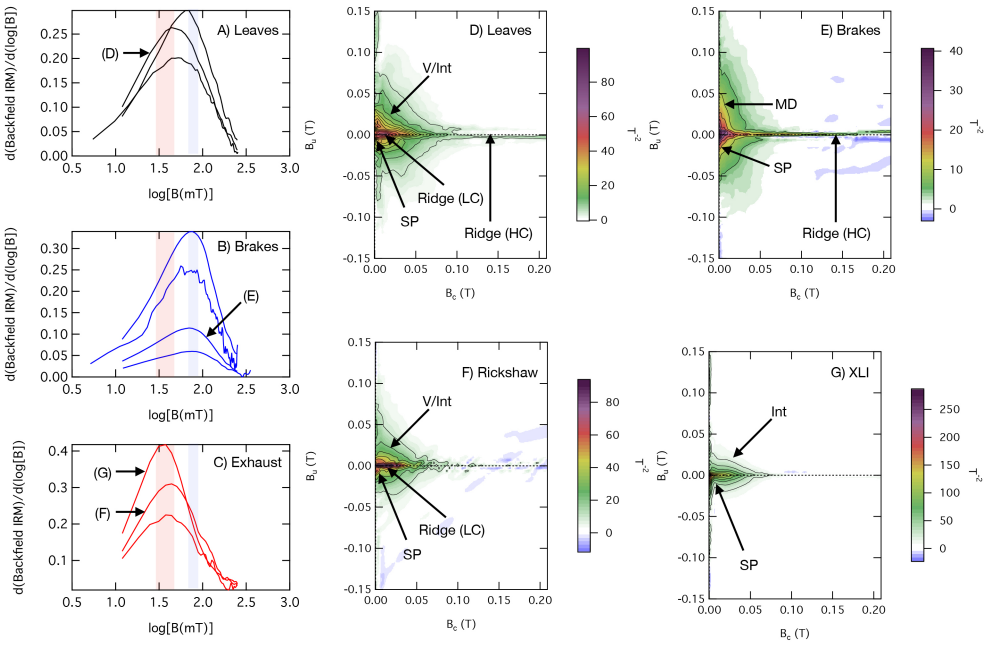

Figure 8 FORC diagrams and their coercivity distribution as a function of log(field). (a-c) Brake pads show the coercivities on the higher end of the distribution spectrum while exhaust pipe specimens are on the lower end. Leaf specimens lie in between both, suggesting it has contribution from both endmembers. (D-G) FORC diagrams have been processed using VARIFORC smoothing (Harrison and Feinberg, 2008) using smoothing parameters S_c,0= 10, S_b,0= 8, S_c,1= S_b, 1= 12, λ : 0.3. D) Average FORC of leaves showing presence of grains in vortex state, a low and high coercivity ridge E) brake pad sample has a distinctive vertical distribution along the Bu axis., indicative of presence MD grains sizes; FORC also shows a sharp SD tail extending to higher coercivity of 150-200 mT, suggestive of contribution from Fe-metal (see Fig. 4a) F) Rickshaw FORC shows a SD fingerprint with a PSD background. (G) XLI petrol exhaust shows interacting grains and an SP ridge. FORC= first-order reversal curve. FORC parameters used were: field step (H) = 1.5 mT, averaging time (t): 300 ms, T=300

4 Discussion

4.1 Sources of non-magnetic particles

Particle size distribution and morphological analysis using SEM/EDX (Fig. 2) show a high contribution to the leaf-deposited particles from non-anthropogenic sources such as mineral dust, dominating the coarser end of the fine-particle spectrum (<2.5 µm). A previous source characterisation study by Stone et al. (2010) in Lahore found that wind-blown mineral dust constituted 74 ± 16% of the coarser $PM_{10\text{-}2.5}$ fraction. In arid areas, the most abundant natural dust mineralogy includes naturally occurring quartz, feldspar, clay minerals and calcium carbonate (Claquin et al. 1999), all of which were observed in our SEM/EDX analysis (Figs. 2A, B, D, E, H). Some proportion of the airborne calcium carbonate particles in Lahore is also likely to be anthropogenic and potentially related to coal power plant, construction industry, and cement production.

Anthropogenic particles such as carbonaceous particles, soot, heavy metals, secondary aerosol particles, and Fe-bearing particles dominate the leaf-deposited particles smaller than < 1 µm. Sources of carbonaceous particles (Fig. 2B) in urban areas have been linked to biomass burning, vehicular combustion, and industry (Saarikoski et al., 2008). In Lahore, carbonaceous and soot particles are likely to be related to fossil fuel combustion in vehicular engines, burning of crops, proximity to brick kilns, industry and/or increased fuelwood burning during winter when demand for heating increases. Heavy metals in Lahore PM likely arise from industrial and vehicular emissions. A pollution characterisation study in Islamabad, Pakistan found high enrichment factors (EF) for Sb, Zn, Cd, Pb, Cu, Co, Cr and Mn and concluded that Co, Cr and Cu were related to metal industries while Pb, Cd and Zn were from vehicular emissions (Shah et al., 2012). Zn, in particular, has been linked to exhaust, tire and road wear, brake wear emissions (Harrison et al., 2012) or smelting processes (Shaheen et al., 2004). The source of Zn in the leaf-deposited PM could be resuspended dust from the nearby traffic and/or from industries in Quaid-e-Azam Industrial or Sundar Industrial Estate. The type of coal influences the chemical composition of fly ash, where lignite-sub bituminous coal has higher levels of Mg-oxides or Ca (e.g., Gaffney and Marley, 2009). Fly ash in Lahore was likely to be anthropogenic and could have originated from coal combustion in the nearby Master coal power plant, brick kilns or domestic use. A focused-ion-beam (FIB) study of fly ash by Chen et al. (2013) found Fe in the core of fly ash spherules, mainly in aluminosilicate phase; while the Fe-bearing particles on the surface were mainly Fe-oxides, as observed in this study.

Calcium sulfate particles observed on the leaves are likely to have an anthropogenic origin from construction activities, cement industry or nearby brick kilns. A previous study by Biswas et al. (2008) in Lahore argued that brick kilns are a major source of sulfate (SO_4^{2-} because of their use of low-grade (sulphur-rich) coal. A reaction of SO_4^{2-} ions with $CaCO_3$ is likely to be a secondary source of calcium sulfate.

K-rich particles have been identified as secondary organic aerosol (SOAs) particles (Fig. 2F) and been related to biomass emissions (Silva et al., 1999) and used as a tracer for burning of crop residues (Neimi et al., 2006). Stubble burning after the harvest of the Kharif (summer) crop is prevalent in both India and Pakistan as farmers prepare to sow wheat for the winter season. Lahore experiences a 'smog season' where haze and fog episodes concurrently occur in October-December. A source apportionment study in Lahore (Lodhi et al., 2009) claimed that during winter crop burning, coal power plants, brick kilns and traffic-related emissions increase the contribution from secondary aerosols in the lower atmosphere—accelerating the formation of fog or smog. A study in Beijing on haze type by Li et al. (2010) argued that particles such as soot, containing ultrafine metallic-Fe, are internally mixed in haze episodes and occur as inclusions within K or S-rich particles. The coating of organic carbon or soot with water-soluble particles such as nitrates of K-rich particles makes them hydrophilic (making them host to UFP), eventually growing larger and more harmful as they are transported further distances (Li et al., 2010).

4.2 Biomagnetic monitoring of Fe-bearing UFPs

Magnetic analysis of leaf, brake pad and exhaust pipe samples indicates the presence of a range of magnetic minerals, varying in their magnetisable content, grain size and morphologies. The results demonstrate that: 1) measured SIRM variations shows that leaf particulate accumulation increases over time (Day 0-26 exposure) within the tree canopies at 1.5 m; and hence can potentially be used for passive biomagnetic monitoring (Fig. S15, supplement); 2) two of the potential sources of magnetic particles on roadside leaves have distinctive FORC signatures and coercivity distributions, and 3) these distinctive source signatures can be recognised in leaf samples, opening up the possibility of effective source attribution using FORC diagrams.

Lahore's average SIRM for year-long exposed leaves was 233 $\times$ 10^{-6} A, 20 days 24.2$\times$ 10^{-6} A, and 40. 1 $\times$ 10^{-6} A for 26 days. These are relatively high compared with average SIRM values at inhalation heights reported in European cities (Table S18, supplement) : 28.83 $\times$ 10^{-6} A (157 days) in Antwerp, Belgium (Hofman et al., 2014), and 81 $\times$ 10^{-6} A in Lancaster, UK (exact exposure days not known but youngest leaves selected at 08/10/07 after in-leaf season; Mitchell et. al., 2009). The SIRM values for leaves from Lahore, Pakistan show a much higher magnetic loading in a lower number of days; however, differences in meteorological parameters, leaf species, deposition velocities and leaf accumulation capacity have not been calibrated against those of European biomagnetic studies, making quantitative comparisons of pollution levels difficult.

We see a temporal and spatial relationship (Fig. 5) with SIRM, indicative of PM depositing on leaves. Roadside vegetation can inhibit airflow and influence nearby air quality by dispersing and/or depositing particulates on vegetation surfaces (Tong et al., 2016), and there is interest in the potential of green infrastructure to act as barriers and air filters when it comes to designing urban spaces. Leaf SIRM values in our study increased both with proximity to a vehicular source and longer exposure time (Fig. 5A). For any given tree, the SIRM observed on the side facing toward the road is higher compared to that facing away from the road, indicating that deposition of PM on roadside leaves dominantly reflects traffic-related air pollution and that PM deposition occurs throughout the leaf canopy but is at a maximum closer to the PM source. Without further data, it is not possible to conclude from this study whether the reduced SIRM magnitude away from the road is due to the 1) 'filtering effect' of trees (Jeanjean et al., 2017) or 2) the increased PM concentrations on the roadside of the vegetation barrier due to reduced air flow (Baldauf et al., 2008). In previous studies, up to 18-20% reduction of PM10 particles using trees has been assessed to mitigate air pollution (Bealey et. al., 2007) and around 50% reduction in indoor PM_{10} (Wang et al., 2019). The proximal/distal SIRM difference is more pronounced for the 26-day data compared to the one-year data, suggesting that magnetic loading may reach a steady-state value after prolonged exposure, irrespective of which side of the tree is sampled.

Leaf samples showed a dampened Verwey transition at 115 K (lower temperature than the expected 120-125 K for stoichiometric magnetite) and rapid drop of remanence between 10-60 K, which is a signature of surface maghmetisation (Ozdemir et al., 1993, Ozdemir and Dunlop, 2009). No direct evidence of metallic Fe was found in the EDX data from leaves, so we assume that oxidised magnetite is the dominant magnetic mineral. It is possible that the primary magnetic source particles are metallic Fe and/or magnetite, both of which are oxidised when exposed to air over time. Magnetic granulometry, LT- vs RT-SIRM and FORC diagrams show a wide mixture of magnetic grain sizes in our samples – from SP ($<$ 30 nm) to SD (30-70 nm) to V (70–700 nm). A higher remanence for FC vs ZFC was observed for all our specimens and is consistent with a) presence of magnetite and b) grains dominated by SD rather than MD behaviour. A previous study by Smirnov (2009) reported magnetite grain-size dependence as a function of the ratio of low-temperature SIRM (RLT at 10 K) for FC and ZFC curves. The ratio for sized PSD particles is close to 1 and 1.27 for acicular magnetite. In our study, RLT was around 1.3 for leaves, and 1.1 for brake-pad and petrol-exhaust pipe specimens – indicating the presence of both PSD and SD magnetite. There is little evidence of a strong MD ($>$ 1 µm) signal in the FORC diagrams, despite direct observation of magnetite spherules $>$ 1 µm in the SEM (e.g., Fig. 3B). This apparent contradiction may be explained by the dendritic form of these magnetite grains, which is likely to reduce the effective grain size to $<$ 1 µm and introduce a strongly interacting component. Our leaf specimens broadly lie on the ISD-MD mixing line of Fig. 7B, rather than the expected ISD-PSD mixing line. Note, however, that this method may be overestimating the MD component due to the presence of a significant SP fraction (identified by the comparison of LT- vs RT-SIRM), which will shift the observed Mrs/Ms from PSD reference values towards MD reference values. The dominant grain size of magnetic particles from specimens in this study are

spread over both interacting and non-interacting fine grain sizes, a wider range compared to what has been previously reported in studies in Lancaster (0.1- 1.0 µm) (Mitchell and Maher, 2009) and Munich (0.1–0.7 m) (Muxworthy et al., 2002).

4.3 Exhaust and Non-exhaust sources

Magnetic granulometry results place our brake-pad specimens near the MD region. Although this matches a MD component visible in the FORC diagrams, and the low bulk coercivity of the brake-pad samples, it fails to reflect the presence of much finer grain-size fractions associated with the presence of a high-coercivity ridge, and the fact that brake-pad residue specimens display the highest coercivity peak in the backfield remanent coercivity distribution plots (Fig. 8B). This failure is partly due to the well-documented problems of using bulk average parameters such as Mrs/Ms to characterise mixtures of different domain states (Roberts et al. 2018), and partly due to the fact that the mixing lines on the granulometric plots are designed for magnetite, whereas FORC diagrams and SEM observations indicate the presence of metallic Fe in the brake pad particles. The high-coercivity ridge that is common to all brake-pad samples can be interpreted in a number of ways. Such ridges are normally associated with non-interacting, uniaxial SD behaviour (Egli et al. 2010). However, these SD signals should also be accompanied by a distinctive -ve/+ve background signal (Newell, 2005), which is absent from the observed brake-pad FORC diagrams. Furthermore, if the high-coercivity ridge signal was due to SD magnetite, and the low-coercivity, vertically spread signal due to MD magnetite, one would expect intermediate grain sizes spanning the V state to create a characteristic tri-lobate signal (Lascu et al. 2018). Such a signal is present in the exhaust samples (e.g., Fig. 8F) but absent from the brake-pad FORCs. The result is a rather unusual bimodal combination of high-coercivity ridge and a low-coercivity, vertically spread signal, which is more consistent with nanoscale particles of metallic Fe (Lappe et al. 2011; Lappe et al. 2013). Micromagnetic simulations by Einsle et al. (2018) demonstrate that both the high-coercivity component of the ridge and the vertically spread signals can be explained by the nucleation and annihilation of vortex states in metallic Fe particles with sizes from 32 nm up to several hundred nanometres. Hysteresis measurements show that the brake-pad specimens have the lowest bulk coercivity values (Fig. S8 and S9, supplement), but the highest distribution of remanence coercivities (Fig. 8B). This observation is explained by the simulations of Einsle et al. (2016), which demonstrate that bulk coercivity values for V-state metallic Fe are extremely low, whereas switching fields associated with V-state nucleation and annihilation are very high. A failure to appreciate this difference may lead to erroneously attributing low-coercivity components in IRM unmixing plots to brake-pad related PM source contributions. The low-coercivity component of the ridge may be generated by SD particles (23-200 nm; Lappe et al. 2011; Muxworthy and Williams 2015), with the region near the origin associated with those particles approaching the SP/SD limit (<23 nm; Nagy et al. 2019). Given the >90% loss of LT-SIRM on heating from 10-300 K (Fig. 6C), a high proportion of particles are expected to be $<$ 23 nm (SP) in size and are likely poorly characterised by our SEM imaging. Our observations support the evidence that brake wear is a major source of Fe-bearing UFPs, which may pose serious risk to human health (Gonet et al. 2021b). For the Toyota XLI exhaust pipe specimen, the steep decrease in RT-SIRM value at 32 K (Fig. 6D) may be related to the presence of pyrrhotite (FeS), (Dekkers et. al., 1989) which can be related to the presence of high-sulfur content in fuel oil. However, ZFC-FC curves do not show such a feature but instead two peaks at 38 K and 42 K, hinting at the presence of some other unidentified magnetic mineral(s).

Magnetic granulometry places the exhaust pipe samples close to the MD (diesel) and PSD (petrol) grain sizes. FORC diagrams of exhaust samples appear more consistent with magnetite spanning the SP-SD-V size range than metallic Fe. Common features include a low-coercivity ridge extending from 0 mT (SP) to 80 mT (SD), and a tri-lobate feature (V and/or magnetic interactions). The FORC diagram of the rickshaw

exhaust (Fig. 8F) most closely resembles those of some leaf samples (Fig. 8D), with near identical peak positions in the backfield remanent coercivity distribution (Fig. 8A, C). Toyota XLI exhaust sample shows a more distinct FORC diagram with a clear SP signature (Lanci and Kent 2018) and an interacting SD signal (Harrison and Lascu 2014). The lack of a V-state tri-lobate feature indicates a finer grain size distribution in comparison to our typical diesel FORCs (Fig S10, supplement). The distinctive nature of the FORC diagrams raises the possibility that FORC diagrams may be capable of not only discriminating between exhaust and non-exhaust emissions, but between different types of exhaust emissions themselves.

The relative uniformity of the backfield remanent coercivity distributions observed in different brake-pad and exhaust-pipe samples contrasts with the more variable, intermediate distributions observed in the different leaf samples. On average, the leaf FORCs more closely resemble those of the exhaust-pipe than the brake-pad samples, although some leaves were observed with a more prominent high coercivity (HC) ridge and backfield remanent coercivity distributions that approach the high values of the brake-pad samples. Together, these observations suggest that the leaf samples represent variable contributions from (at least) these two sources, and that (in principle) the contributions from each could be quantified using approaches such as FORC-PCA (Lascu et al. 2015; Harrison et al. 2018). Two complications that would need to be addressed first, however, are i) the relatively high noise levels of the FORC data for such weak samples, and ii) the possibility that metallic-Fe particles generated by brake wear become oxidised over time, so that their contribution to the FORC diagram of a leaf sample is modified relative to that in the pure brake-pad end member. These issues will be tackled in a future study.

Specimen	T_v (K)	$[RT\text{-}SIRM]_{10K}$ (Am^2 10^{-6})	$[LT\text{-}SIRM]_{10K}$ (ZFC) (Am^2 10^{-6})	SP fraction (%)*	$[RT\text{-}SIRM]_{MAX}$ (Am^2 10^{-6})	T at $[RT\text{-}SIRM]_{MAX}$ (K)	$[RT\text{-}SIRM\text{-}cooling]_{MIN}$ (Am^2 10^{-6})	Remanence loss (%)**
XLI-Brake pad	-	0.123	1.61	92.36	0.124	150	0.117	5.65
XLI- exhaust pipe	-	0.210	1.37	84.67	0.215	150	0.196	8.84

*$[LT\text{-}SRIM]_{10K} - [RT\text{-}SIRM]_{10K}$/ $[LT\text{-}SRIM]_{10K}$ x100 **$[RT\text{-}SIRM]_{MAX}$- $[RT\text{-}SIRM]_{MIN}$/[$RT\text{-}SIRM]_{MAX}$ x100

Table 1A

Specimen	T_v (K)	$[RT\text{-}SIRM]_{10K}$ ($Am^2\,kg^{-1}$ 10^{-6})	$[LT\text{-}SIRM]_{10K}$ (ZFC) ($Am^2\,kg^{-1}$ 10^{-6})	SP fraction (%)*	$[RT\text{-}SIRM]_{MAX}$ ($Am^2\,kg^{-1}$ 10^{-6})	T at $[RT\text{-}SIRM]_{MAX}$ (K)	$[RT\text{-}SIRM\text{-}cooling]_{MIN}$ ($Am^2\,kg^{-1}$ 10^{-6})	Remanence loss (%)**
T10_TSL_1Y	115	104.0	240	56.60	129	200	104.0	19.37
T10_TSL_20d	115	105.5	295	64.40	122	200	105.5	13.52

*$[LT\text{-}SRIM]_{10K} - [RT\text{-}SIRM]_{10K}$/ $[LT\text{-}SRIM]_{10K}$ x100 **$[RT\text{-}SIRM]_{MAX}$- $[RT\text{-}SIRM]_{MIN}$/[$RT\text{-}SIRM]_{MAX}$ x100

Table 1B

Table 1A and B Room and low-temperature measurements for exhaust, non-exhaust, and leaf specimens. The contribution of superparamagnetic grains is given by $[LT\text{-}SRIM]_{10K} - [RT\text{-}SIRM]_{10K}$/ [LT-SRIM]10K and loss of remanence from peak SIRM at room temperature is given by $[RT\text{-}SIRM]_{MAX}$- $[RT\text{-}SIRM]_{MIN}$/[$RT\text{-}SIRM]_{MAX}$

4.4 Outlook

Fe-bearing nanoparticles are highly toxic; for example, magnetite's bioreactive Fe2+ may disrupt the redox balance and damage cells (Maher et al., 2020); the presence of Fe-catalysed free radicals have been linked to increasing oxidative damage in development of Alzheimer's disease. A recent study on brake abrasion dust (BAD) shows that particles from brake pads with metallic content (abundant in Fe) provoke an inflamma-

tory response in human airways (Selly et al., 2020). Observations from the SEM also show the association of nano-sized Fe-particles with transition metals, and toxicological studies have suggested that metal-rich UFPs have been able to access all major organs (Nel et al., 2006), and cause acute pulmonary health implications. (Deher and Jascot, 1997). The nature of nano-sized particles is such that humans are susceptible to their exposure and the higher toxicity of metals, such as Fe. For this reason, it is essential that their contribution in ambient PM is quantified across the urban environment where most people are most exposed to them. Magnetic measurements are an effective way to detect the presence of and differentiate between these particles. The variation in magnetic signatures of exhaust and non-exhaust sources as observed in FORCs, low-temperature magnetic measurements and microscopy shows the potential importance of the technique to quantify the contributions from these sources. As the world tackles climate change and air pollution, countries are pushing for a transition to electric vehicles (EV)— although a move to EV will bring exhaust emissions to near-zero, the relative contribution from non-exhaust (brake, tyre, and road wear) sources is likely to increase. The methods outlined here may provide a cost-effective way to monitor the changing contributions to roadside particulate pollution levels over the coming decades.

5 Conclusions

Lahore is the second most polluted city in the world in terms of $PM_{2.5}$ and PM_{10}, but the largest weight fraction of such particles constitutes of mineral dust and carbonaceous particles. Recent epidemiological studies have revealed acute health concerns arising from exposure to UFP and toxic heavy metals such as Fe; highlighting the need to quantify and characterise this particle size fraction. Using magnetic protocols and high-resolution microscopy, we have been able to characterise the composition, size and origin of PM deposited on roadside leaves, and to distinguish between two major traffic-related sources of PM in Lahore. SEM and EDX data show that Fe-bearing particles are mainly oxidised magnetite and Fe-metal, contributing to the magnetic signal in our roadside leaves. Our FORC results show distinctive fingerprints for exhaust and brake wear residue particulates, which appear to be the two major contributions to the magnetic signal on the leaves. We confirm the presence of a significant nano-sized ferrimagnetic fraction both on the roadside leaves and in the exhaust and brake wear samples by conducting low-temperature magnetic measurements. The SP contribution of these nanoparticles is not observable in SEM or room-temperature magnetic methods, but these nano-sized particles may have serious health implications. PM levels reported by traditional, mass-based metric systems are quick and real-time, but they fail to take into account the complex compositions, morphologies and interactions of particulates, and especially of the nanoparticles, with serious potential implications in adverse health outcomes including cardiovascular, respiratory and neurodegenerative diseases. Our magnetic and microscopy data identify the potential for increased magnetic quantification and differentiation of PM sources at a range of spatial and temporal scales.

Acknowledgments

HAS would like to thank Muhammad Rafiq, local gardener in Lahore who knew everything about the trees on Canal Bank Road; Dr. Iris Buisman for help with coating samples and SEM sessions; Dr Cheng Liu at Maxwell Centre for training me on the MPMS. HAS would also like to thank Plant Health Protection Authority in Lahore, Pakistan for providing a phytosanitary certificate for the leaf specimens and the Cambridge Trust for funding.

6 Availability statement

The magnetic raw data measured at room and low temperature is available at Zenodo via [https://doi.org/10.5281/zenodo.5733952] with open access.

7 References

Araviiskaia, E., Berardesca, E., Bieber, T., Gontijo, G., Sanchez Viera, M., Marrot, L. et al. (2019). The impact of airborne pollution on skin. Journal Of The European Academy Of Dermatology And Venereology, 33(8), 1496-1505. doi: 10.1111/jdv.15583

Baldauf, R., Thoma, E., Khlystov, A., Isakov, V., Bowker, G., Long, T., Snow, R. (2008). Impacts of noise barriers on near-road air quality. Atmospheric Environment, 42(32), 7502-7507. doi: 10.1016/j.atmosenv.2008.05.051

Bealey, W., McDonald, A., Nemitz, E., Donovan, R., Dragosits, U., Duffy, T., Fowler, D. (2007). Estimating the reduction of urban PM10 concentrations by trees within an environmental information system for planners. Journal Of Environmental Management, 85(1), 44-58. doi: 10.1016/j.jenvman.2006.07.007

Biswas, K., Ghauri, B., Husain, L. (2008). Gaseous and aerosol pollutants during fog and clear episodes in South Asian urban atmosphere. Atmospheric Environment, 42(33), 7775-7785. doi: 10.1016/j.atmosenv.2008.04.056

Buseck, P., Adachi, K. (2008). Nanoparticles in the Atmosphere. Elements, 4(6), 389-394. doi: 10.2113/gselements.4.6.389

Buseck, P., Adachi, K., Gelencsér, A., Tompa, É., Pósfai, M. (2014). Ns-Soot: A Material-Based Term for Strongly Light-Absorbing Carbonaceous Particles. Aerosol Science And Technology, 48(7), 777-788. doi: 10.1080/02786826.2014.919374

Calderón-Garcidueñas, L., González-Maciel, A., Mukherjee, P., Reynoso-Robles, R., Pérez-Guillé, B., Gayosso-Chávez, C. et al. (2019). Combustion- and friction-derived magnetic air pollution nanoparticles in human hearts. Environmental Research, 176, 108567. doi: 10.1016/j.envres.2019.108567

Calderón-Garcidueñas, L., González-Maciel, A., Reynoso-Robles, R., Hammond, J., Kulesza, R., Lachmann, I. et al. (2020). Quadruple abnormal protein aggregates in brainstem pathology and exogenous metal-rich magnetic nanoparticles (and engineered Ti-rich nanorods). The substantia nigrae is a very early target in young urbanites and the gastrointestinal tract a key brainstem portal. Environmental Research, 191, 110139. doi: 10.1016/j.envres.2020.110139

Calderón-Garcidueñas, L., Reynoso-Robles, R., Vargas- Martínez, J., Gómez-Maqueo-Chew, A., Pérez-Guillé, B., Mukherjee, P. et al. (2016). Prefrontal white matter pathology in air pollution exposed Mexico City young urbanites and their potential impact on neurovascular unit dysfunction and the development of Alzheimer's disease. Environmental Research, 146, 404-417. doi: 10.1016/j.envres.2015.12.031

Chen, H., Grassian, V., Saraf, L., Laskin, A. (2013). Chemical imaging analysis of environmental particles using the focused ion beam/scanning electron microscopy technique: microanalysis insights into atmospheric chemistry of fly ash. The Analyst, 138(2), 451-460. doi: 10.1039/c2an36318f

Chen, H., Kwong, J., Copes, R., Tu, K., Villeneuve, P., van Donkelaar, A. et al. (2017). Living near major roads and the incidence of dementia, Parkinson's disease, and multiple sclerosis: a population-based cohort study. The Lancet, 389(10070), 718-726. doi: 10.1016/s0140-6736(16)32399-6

Chen, X., Zhang, X., Zhang, X. (2017). Smog in Our Brains: Gender Differences in the Impact of Exposure to Air Pollution on Cognitive Performance. SSRN Electronic Journal. doi: 10.2139/ssrn.2940618

Claquin, T., Schulz, M., Balkanski, Y. (1999). Modeling the mineralogy of atmospheric dust sources. Journal Of Geophysical Research: Atmospheres, 104(D18), 22243-22256. doi: 10.1029/1999jd900416

Coelho, A. (2018). TOPASandTOPAS-Academic: an optimization program integrating computer algebra and crystallographic objects written in C++. Journal Of Applied Crystallography, 51(1), 210-218. doi: 10.1107/s1600576718000183

Cornell, R. and Schwertmann, U., 1996. The iron oxides. Weinheim: VCH. Dai, Q., Zhou, M., Li, H., Qian, X., Yang, M., Li, F. (2020). Biomagnetic monitoring combined with support vector machine: a new opportunity for predicting particle-bound-heavy metals. Scientific Reports, 10(1). doi: 10.1038/s41598-020-65677-8

Dankers, P. H (1978). Magnetic properties of dispersed natural iron oxides of known grain size, PhD thesis, University of Utrecht. Dekkers, M., Mattéi, J., Fillion, G., Rochette, P. (1989). Grain-size dependence of the magnetic behavior of pyrrhotite during its low-temperature transition at 34 K. Geophysical Research Letters, 16(8), 855-858. doi: 10.1029/gl016i008p00855

Devlin, R., Smith, C., Schmitt, M., Rappold, A., Hinderliter, A., Graff, D., Carraway, M. (2014). Controlled Exposure of Humans with Metabolic Syndrome to Concentrated Ultrafine Ambient Particulate Matter Causes Cardiovascular Effects. Toxicological Sciences, 140(1), 61-72. doi: 10.1093/toxsci/kfu063

Dollase, W.A. (1986). Correction of intensities for preferred orientation in powder diffractometry: application of the March model. Journal Of Applied Crystallography, 19(4), 267-272. doi: 10.1107/s0021889886089458

Dreher, K.L., Jaskot, R.H. et al., (1997). Soluble transition metals mediate residual oil fly ash induced acute lung injury. Journal Of Toxicology and Environmental Health, 50(3), 285-305. doi: 10.1080/009841097160492

Dunlop, D. (1973). Superparamagnetic and single-domain threshold sizes in magnetite. Journal Of Geophysical Research, 78(11), 1780-1793. doi: 10.1029/jb078i011p01780

Dusseldorp, A., Kruize, H., Brunekreef, B., Hofschreuder, P., de Meer, G., van Oudvorst, A. (1995). Associations of PM10 and airborne iron with respiratory health of adults living near a steel factory. American Journal Of Respiratory And Critical Care Medicine, 152(6), 1932-1939. doi: 10.1164/ajrccm.152.6.8520758 E Egli, R. (2013). VARIFORC: An optimized protocol for calculating non-regular first-order reversal curve (FORC) diagrams. Global And Planetary Change, 110, 302-320. doi: 10.1016/j.gloplacha.2013.08.003

Einsle, J. F., Harrison, R. J., Kasama, T., Conbhuí, P. Ó., Fabian, K., Williams, W., ... Midgley, P. A. (2016). Multi-scale three-dimensional characterization of iron particles in dusty olivine: Implications for paleomagnetism of chondritic meteorites. American Mineralogist, 101(9). https://doi.org/10.2138/am-2016-5738CCBY

Einsle, J., Eggeman, A., Martineau, B., Saghi, Z., Collins, S., Blukis, R. et al. (2018). Nanomagnetic properties of the meteorite cloudy zone. Proceedings Of The National Academy Of Sciences, 115(49), E11436-E11445. doi: 10.1073/pnas.1809378115

Franceschi, V., (2001). Calcium oxalate in plants. Trends in Plant Science, 6(7), p.331.

Gaffney, J., Marley, N. (2009). The impacts of combustion emissions on air quality and climate – From coal to biofuels and beyond. Atmospheric Environment, 43(1), 23-36. doi: 10.1016/j.atmosenv.2008.09.016

Glasauer, S.M., Beveridge, T.J., Burford, E.P, Harper, F.A., Gadd, G.M. (2013). Metals and Metalloids, Transformation by Microorganisms, Reference Module in Earth Systems and Environmental Sciences, Elsevier.

Gonet, T., Maher, B. (2019). Airborne, Vehicle-Derived Fe-Bearing Nanoparticles in the Urban Environment: A Review. Environmental Science Technology, 53(17), 9970-9991. doi: 10.1021/acs.est.9b01505

Gonet, T., Maher, B., Kukutschová, J. (2021a). Source apportionment of magnetite particles in roadside airborne particulate matter. Science Of The Total Environment, 752, 141828. doi: 10.1016/j.scitotenv.2020.141828

Gonet, T., Maher, B., Nyirő-Kósa, I., Pósfai, M., Vaculík, M., Kukutschová, J. (2021b). Size-resolved, quantitative evaluation of the magnetic mineralogy of airborne brake-wear particulate emissions. Environmental Pollution, 288, 117808. doi: 10.1016/j.envpol.2021.117808

Harrison, R. J., Lascu, I. (2014). FORCulator: A micromagnetic tool for simulating first-order reversal curve diagrams. Geochemistry, Geophysics, Geosystems, 15(12), 4671–4691. doi: 10.1002/2014GC005582

Harrison, R., Feinberg, J. (2008). FORCinel: An improved algorithm for calculating first-order reversal curve distributions using locally weighted regression smoothing. Geochemistry, Geophysics, Geosystems, 9(5), doi: 10.1029/2008gc001987

Harrison, R., Jones, A., Gietl, J., Yin, J., Green, D. (2012). Estimation of the Contributions of Brake Dust, Tire Wear, and Resuspension to Nonexhaust Traffic Particles Derived from Atmospheric Measurements. Environmental Science Technology, 46(12), 6523-6529. doi: 10.1021/es300894r

Harrison, R., Muraszko, J., Heslop, D., Lascu, I., Muxworthy, A., Roberts, A. (2018). An Improved Algorithm for Unmixing First-Order Reversal Curve Diagrams Using Principal Component Analysis. Geochemistry, Geophysics, Geosystems, 19(5), 1595-1610. doi: 10.1029/2018gc007511

Hellenbrandt, M. (2004). The Inorganic Crystal Structure Database (ICSD)—Present and Future. Crystallography Reviews, 10(1), 17-22. doi: 10.1080/08893110410001664882

Hofman, J., Castanheiro, A., Nuyts, G., Joosen, S., Spassov, S., Blust, R. et al. (2020). Impact of urban street canyon architecture on local atmospheric pollutant levels and magneto-chemical PM10 composition: An experimental study in Antwerp, Belgium. Science Of The Total Environment, 712, 135534. doi: 10.1016/j.scitotenv.2019.135534

Hofman, J., Wuyts, K., Van Wittenberghe, S., Samson, R. (2014). On the temporal variation of leaf magnetic parameters: Seasonal accumulation of leaf-deposited and leaf-encapsulated particles of a roadside tree crown. Science Of The Total Environment, 493, 766-772. doi: 10.1016/j.scitotenv.2014.06.074

Jeanjean, A., Buccolieri, R., Eddy, J., Monks, P., Leigh, R. (2017). Air quality affected by trees in real street canyons: The case of Marylebone neighbourhood in central London. Urban Forestry Urban Greening, 22, 41-53. doi: 10.1016/j.ufug.2017.01.009

Kardel, F., Wuyts, K., Maher, B., Hansard, R., Samson, R. (2011). Leaf saturation isothermal remanent magnetization (SIRM) as a proxy for particulate matter monitoring: Inter-species differences and in-season variation. Atmospheric Environment, 45(29), 5164-5171. doi: 10.1016/j.atmosenv.2011.06.025

Kasama, T., Church, N. S., Feinberg, J., Dunin-Borkowski, R., Harrison, R. (2010). Direct observation of ferrimagnetic/ferroelastic domain interactions in magnetite below the Verwey transition. Earth and Planetary Science Letters, 297(1–2), 10–17. Retrieved from doi: 10.1016/j.epsl.2010.05.004

Kelly, F., Fussell, J. (2012). Size, source and chemical composition as determinants of toxicity attributable to ambient particulate matter. Atmospheric Environment, 60, 504-526. doi: 10.1016/j.atmosenv.2012.06.039

Kojima, T., Buseck, P., Iwasaka, Y., Matsuki, A., Trochkine, D. (2006). Sulfate-coated dust particles in the free troposphere over Japan. Atmospheric Research, 82(3-4), 698-708. doi: 10.1016/j.atmosres.2006.02.024

Lagroix, F., Guyodo, Y. (2017). A New Tool for Separating the Magnetic Mineralogy of Complex Mineral Assemblages from Low Temperature Magnetic Behavior. Frontiers In Earth Science, 5. doi: 10.3389/feart.2017.00061

Lanci, L., Kent, D. V. (2018). Forward Modeling of Thermally Activated Single-Domain Magnetic Particles Applied to First-Order Reversal Curves. Journal of Geophysical Research: Solid Earth, 123(5), 3287–3300. https://doi.org/10.1002/2018JB015463

Lappe, S.-C. L. L., Church, N. S., Kasama, T., da Silva Fanta, A. B., Bromiley, G., Dunin-Borkowski, R. E., ... Harrison, R. J. (2011). Mineral magnetism of dusty olivine: A credible recorder of pre-accretionary remanence. Geochemistry, Geophysics, Geosystems, 12(12), Q12Z35. doi: 10.1029/2011GC003811

Lappe, S.-C. L. L., Feinberg, J. M., Muxworthy, A., Harrison, R. J. (2013). Comparison and calibration of nonheating paleointensity methods: A case study using dusty olivine. Geochemistry, Geophysics, Geosystems, 14(7), 2143–2158. doi: /10.1002/ggge.20141

Lascu, I., Banerjee, S., Berquó, T. (2010). Quantifying the concentration of ferrimagnetic particles in sediments using rock magnetic methods. Geochemistry, Geophysics, Geosystems, 11(8), doi: 10.1029/2010gc003182

Lehndorff, E., Schwark, L. (2004). Biomonitoring of air quality in the Cologne Conurbation using pine needles as a passive sampler—Part II: polycyclic aromatic hydrocarbons (PAH). Atmospheric Environment, 38(23), 3793-3808. doi: 10.1016/j.atmosenv.2004.03.065

Leitte, A., Schlink, U., Herbarth, O., Wiedensohler, A., Pan, X., Hu, M. et al. (2012). Associations between size-segregated particle number concentrations and respiratory mortality in Beijing, China. International Journal Of Environmental Health Research, 22(2), 119-133. doi: 10.1080/09603123.2011.605878

Li, W., Shao, L. (2009). Transmission electron microscopy study of aerosol particles from the brown hazes in northern China. Journal Of Geophysical Research, 114(D9). doi: 10.1029/2008jd011285

Li, W., Shao, L., Buseck, P. (2010). Haze types in Beijing and the influence of agricultural biomass burning. Atmospheric Chemistry And Physics, 10(17), 8119-8130. doi: 10.5194/acp-10-8119-2010

Lodhi, A., Ghauri, B., Khan, M., Rahman, S., Shafique, S. (2009). Particulate matter (PM2.5) concentration and source apportionment in Lahore. Journal Of The Brazilian Chemical Society, 20(10), 1811-1820. doi: 10.1590/s0103-50532009001000007

Madsen, I.C., Scarlett, N.V.Y. (2008). Quantitative Phase Analysis. In Powder Diffraction: Theory and Practice, edited by Dinnabier, R.E., Royal Society of Chemistry.

Maher, B. (1988). Magnetic properties of some synthetic sub-micron magnetites. Geophysical Journal International, 94(1), 83-96. doi: 10.1111/j.1365-246x.1988.tb03429.x

Maher, B., Thompson, R. (1999). Quaternary climates, environments and magnetism. Cambridge: Cambridge University Press.

Maher, B., Ahmed, I., Karloukovski, V., MacLaren, D., Foulds, P., Allsop, D. et al. (2016). Magnetite pollution nanoparticles in the human brain. Proceedings Of The National Academy Of Sciences, 113(39), 10797-10801. doi: 10.1073/pnas.1605941113

Maher, B., González-Maciel, A., Reynoso-Robles, R., Torres-Jardón, R., Calderón-Garcidueñas, L. (2020). Iron-rich air pollution nanoparticles: An unrecognised environmental risk factor for myocardial mitochondrial dysfunction and cardiac oxidative stress. Environmental Research, 188, 109816. doi: 10.1016/j.envres.2020.109816

Maher, B., Moore, C., Matzka, J. (2008). Spatial variation in vehicle-derived metal pollution identified by magnetic and elemental analysis of roadside tree leaves. Atmospheric Environment, 42(2), 364-373. doi: 10.1016/j.atmosenv.2007.09.013

Matzka, J., Maher, B. (1999). Magnetic biomonitoring of roadside tree leaves: identification of spatial and temporal variations in vehicle-derived particulates. Atmospheric Environment, 33(28), 4565-4569. doi: 10.1016/s1352-2310(99)00229-0

Miller, M., Raftis, J., Langrish, J., McLean, S., Samutrtai, P., Connell, S. et al. (2017). Correction to"Inhaled Nanoparticles Accumulate at Sites of Vascular Disease". ACS Nano, 11(10), 10623-10624. doi: 10.1021/acsnano.7b06327

Mitchell, R., Maher, B. (2009). Evaluation and application of biomagnetic monitoring of traffic-derived particulate pollution. Atmospheric Environment, 43(13), 2095-2103. doi: 10.1016/j.atmosenv.2009.01.042

Moskowitz, B., Frankel, R., Bazylinski, D., Jannasch, H., Lovley, D. (1989). A comparison of magnetite particles produced anaerobically by magnetotactic and dissimilatory iron-reducing bacteria. Geophysical Research Letters, 16(7), 665-668. doi: 10.1029/gl016i007p00665

Muxworthy, A. R., Williams, W. (2015). Critical single-domain grain sizes in elongated iron particles: implications for meteoritic and lunar magnetism. Geophysical Journal International, 202(1), 578–583. https://doi.org/10.1093/gji/ggv180

Muxworthy, A.R, Matzka, J., Davila, A., Petersen, N. (2003). Magnetic signature of daily sampled urban atmospheric particles. Atmospheric Environment, 37(29), 4163-4169. doi: 10.1016/s1352-2310(03)00500-4

Muxworthy, A.R., Schmidbauer, E., Petersen, N. (2002). Magnetic properties and Mössbauer spectra of urban atmospheric particulate matter: a case study from Munich, Germany. Geophysical Journal International, 150(2), 558-570. doi: 10.1046/j.1365-246x.2002.01725.x

Nagy, L., Williams, W., Tauxe, L., Muxworthy, A. R., Ferreira, I. (2019). Thermomagnetic recording fidelity of nanometer-sized iron and implications for planetary magnetism. Proceedings of the National Academy of Sciences, 116(6), 1984–1991. doi: 10.1073/pnas.1810797116

Nel, A., Xia, T., Madler, L., Li, N. (2006). Toxic Potential of Materials at the Nanolevel. Science, 311(5761), 622-627. doi: 10.1126/science.1114397 Newell, A. J. (2005). A high-precision model of first-order reversal curve (FORC) functions for single-domain ferromagnets with uniaxial anisotropy. Geochemistry, Geophysics, Geosystems, 6(5), Q05010. doi: 10.1029/2004GC000877

Ohlwein, S., Kappeler, R., Kutlar Joss, M., Künzli, N., Hoffmann, B. (2019). Health effects of ultrafine particles: a systematic literature review update of epidemiological evidence. International Journal of Public Health, 64(4), 547-559. doi: 10.1007/s00038-019-01202-7

Özdemir, Ö., Banerjee, S. (1982). A preliminary magnetic study of soil samples from west-central Minnesota. Earth And Planetary Science Letters, 59(2), 393-403. doi: 10.1016/0012-821x(82)90141-8

Özdemir, Ö., Dunlop, D., Moskowitz, B. (1993). The effect of oxidation on the Verwey transition in magnetite. Geophysical Research Letters, 20(16), 1671-1674. doi: 10.1029/93gl01483

Penttinen, P., Timonen, K., Tiittanen, P., Mirme, A., Ruuskanen, J., Pekkanen, J. (2001). Ultrafine particles in urban air and respiratory health among adult asthmatics. European Respiratory Journal, 17(3), 428-435. doi: 10.1183/09031936.01.17304280

Pike, C., Roberts, A., Verosub, K. (1999). Characterizing interactions in fine magnetic particle systems using first order reversal curves. Journal Of Applied Physics, 85(9), 6660-6667. doi: 10.1063/1.370176

Roberts, A. P., Tauxe, L., Heslop, D., Zhao, X., Jiang, Z. (2018). A Critical Appraisal of the 'Day' Diagram. Journal of Geophysical Research: Solid Earth. doi: 10.1002/2017JB015247

Roberts, A., Pike, C., Verosub, K. (2000). First-order reversal curve diagrams: A new tool for characterizing the magnetic properties of natural samples. Journal Of Geophysical Research: Solid Earth, 105(B12), 28461-28475. doi: 10.1029/2000jb900326

Rückerl, R., Schneider, A., Breitner, S., Cyrys, J., Peters, A. (2011). Health effects of particulate air pollution: A review of epidemiological evidence. Inhalation Toxicology, 23(10), 555-592. doi: 10.3109/08958378.2011.593587

Saarikoski, S., Timonen, H., Saarnio, K., Aurela, M., Järvi, L., Keronen, P. et al. (2008). Sources of organic carbon in fine particulate matter in northern European urban air. Atmospheric Chemistry And Physics, 8(20), 6281-6295. doi: 10.5194/acp-8-6281-2008

Sagnotti, L., Macrì, P., Egli, R., Mondino, M. (2006). Magnetic properties of atmospheric particulate matter from automatic air sampler stations in Latium (Italy): Toward a definition of magnetic fingerprints for natural and anthropogenic PM10sources. Journal Of Geophysical Research: Solid Earth, 111(B12). doi: 10.1029/2006jb004508

Sagnotti, L., Taddeucci, J., Winkler, A., Cavallo, A. (2009). Compositional, morphological, and hysteresis characterization of magnetic airborne particulate matter in Rome, Italy. Geochemistry, Geophysics, Geosystems, 10(8). doi: 10.1029/2009gc002563

Schraufnagel, D. E. (2020). 'The health effects of ultrafine particles', Experimental and Molecular Medicine. doi: 10.1038/s12276-020-0403-3

Schwarze, P., Øvrevik, J., Låg, M., Refsnes, M., Nafstad, P., Hetland, R., Dybing, E. (2006). Particulate matter properties and health effects: consistency of epidemiological and toxicological studies. Human Experimental Toxicology, 25(10), 559-579. doi: 10.1177/096032706072520

Seaton, A., Godden, D., MacNee, W., Donaldson, K. (1995). Particulate air pollution and acute health effects. The Lancet, 345(8943), 176-178. doi: 10.1016/s0140-6736(95)90173-6

Selley, L., Schuster, L., Marbach, H., Forsthuber, T., Forbes, B., Gant, T. et al. (2020). Brake dust exposure exacerbates inflammation and transiently compromises phagocytosis in macrophages. Metallomics, 12(3), 371-386. doi: 10.1039/c9mt00253g

Shah, M., Shaheen, N., Nazir, R. (2012). Assessment of the trace elements level in urban atmospheric particulate matter and source apportionment in Islamabad, Pakistan. Atmospheric Pollution Research, 3(1), 39-45. doi: 10.5094/apr.2012.003 Shi, Z., Shao, L., Jones, T., Whittaker, A., Lu, S., Bérubé, K. et al. (2003). Characterization

of airborne individual particles collected in an urban area, a satellite city and a clean air area in Beijing, 2001. Atmospheric Environment, 37(29), 4097-4108. doi: 10.1016/s1352-2310(03)00531-4

Silva, P., Liu, D., Noble, C., Prather, K. (1999). Size and Chemical Characterization of Individual Particles Resulting from Biomass Burning of Local Southern California Species. Environmental Science Technology, 33(18), 3068-3076. doi: 10.1021/es980544p

Smirnov, A. (2009). Grain size dependence of low-temperature remanent magnetization in natural and synthetic magnetite: Experimental study. Earth, Planets And Space, 61(1), 119-124. doi: 10.1186/bf03352891

Smith, M., Harris, P., Sayre, L., Perry, G. (1997). Iron accumulation in Alzheimer disease is a source of redox-generated free radicals. Proceedings Of The National Academy Of Sciences, 94(18), 9866-9868. doi: 10.1073/pnas.94.18.9866 Spassov, S., Egli, R., Heller, F., Nourgaliev, D., Hannam, J. (2004). Magnetic quantification of urban pollution sources in atmospheric particulate matter. Geophysical Journal International, 159(2), 555-564. doi: 10.1111/j.1365-246x.2004.02438.x

Stone, E., Schauer, J., Quraishi, T., Mahmood, A. (2010). Chemical characterization and source apportionment of fine and coarse particulate matter in Lahore, Pakistan. Atmospheric Environment, 44(8), 1062-1070. doi: 10.1016/j.atmosenv.2009.12.015

Tong, Z., Baldauf, R., Isakov, V., Deshmukh, P., Max Zhang, K. (2016). Roadside vegetation barrier designs to mitigate near-road air pollution impacts. Science Of The Total Environment, 541, 920-927. doi: 10.1016/j.scitotenv.2015.09.067 Verwey E.J.W., (1939). Electronic conduction of magnetite (Fe3O4) and its transition point at low temperatures, Nature, 144, 327. doi: 10.1038/144327b0

Wang, H., Maher, B., Ahmed, I., Davison, B. (2019). Efficient Removal of Ultrafine Particles from Diesel Exhaust by Selected Tree Species: Implications for Roadside Planting for Improving the Quality of Urban Air. Environmental Science Technology, 53(12), 6906-6916. doi: 10.1021/acs.est.8b06629

Yang, Y., Vance, M., Tou, F., Tiwari, A., Liu, M., Hochella, M. (2016). Nanoparticles in road dust from impervious urban surfaces: distribution, identification, and environmental implications. Environmental Science: Nano, 3(3), 534-544. doi: 10.1039/c6en00056h

Yuan, Y., Wu, Y., Ge, X., Nie, D., Wang, M., Zhou, H., Chen, M. (2019). In vitro toxicity evaluation of heavy metals in urban air particulate matter on human lung epithelial cells. Science Of The Total Environment, 678, 301-308. doi: 10.1016/j.scitotenv.2019.04.431

Figure 1. (A) Location of area of study and the nearby industrial estates and brick kilns. (B) Area of study showing the sampled trees and their distance from Canal bank road and the service lane.

Figure 2. SEM images of adaxial side of leaves. (A) Secondary electron (SE) image of fly ash particles clustered with Zn-rich spherical particle and Fe-bearing particle associated with Ca-sulfate agglomerate. (B) BSE image of a calcium-sulfate agglomerate clustered together with fly ash having many Fe-bearing ultrafine particles on its surface. (C) Smooth platy-like gypsum particle. (D) Spherical pollen grains. (E) Smooth spherical fly ash particle. (F) K-rich rectangular particle. (G) Chain-like aggregate of soot particles. (H) Rectangular plagioclase, and a spherical carbonaceous particle. (Blue border: BSE, Yellow border: SE)

Figure 3. SEM images and EDX maps of Fe-bearing particles. (A) Cluster of Fe metal particles, ranging from 2.5 µm to less than 1 µm, embedded on surface of an Al-silicate; they exhibit a spiky ball morphology. (B) A spherical Fe-oxide particle (possibly from high temperature combustion reaction sitting on top of an Al-silicate. (C) Clusters of micron-sized Fe particles and a few discrete nanoparticles appear to be physically enclosed within a silicate particle. (D) Nano-sized Fe-bearing particles embedded within a silicate and carbonaceous agglomerate. [All images are BSE]

Figure 4. (A) Brake pad samples of XLI, showing nano-sized Fe-metal particles within silicate. EDX spectra for particles [1] shows the presence of metallic Fe and [2] oxidised Fe. (B) XLI petrol exhaust showing irregular morphology of Fe particles; EDX spectra of particle [3] shows Fe-bearing particle embedded on top of a silicate (C) BSE image of Mazda truck 3.5 L diesel exhaust pipe showing nano-sized Fe-particles embedded on top of a silicate mineral and the corresponding EDX map [4] shows the presence of sulfur with Fe-bearing particles.

Figure 5. (A) Temporal and Spatial variation on measured leaf specimens (see Fig. 1B for Tree positions). (B) shows the average SIRM values of leaf specimens over different timescales

Figure 6. A 2.5 T field was applied to our samples to get room-temperature saturation isothermal magnetic remanence (RT-SIRM). The samples were then cycled from 300 K to 10 K and back to 300 K in zero-field, giving us two curves: RT-SIRM (cooling- 300- 10 K) and RT-SIRM (warming – 10 K to 300K). ZFC-FC warming curves where IRM for FC was acquired at 2.5 T at 10 K. ZFC-FC curves show a peak at Verwey transition for leaf specimens at 115 K. RT-SIRM cooling curve for XLI exhaust shows a peak at around 32 K, possible hint at pyrrhotite. Leaf specimens T10-1Y-TSL and T10-20d-TSL are mass normalised by dry weigh of leaf powder measured using the gel cap; an accurate mass normalisation was not possible for brake and exhaust-pipe specimens; therefore, absolute moment values are reported for them. Values for -dM/dT vs temperature graph were taken from 12 K instead of 10 K because the temperature was not stabilised at low temperatures, hence contributing to slight curvature in -dM/dT at 10-12 K.

Figure 7. A) shows a comparison of leaf, brake pad and exhaust pipe specimens with sized magnetite grains (Maher, 1988; Dankers, 1978; Özdemir and Banerjee, 1982). This is represented by room temperature ARM susceptibility normalised by saturation isothermal remanent magnetisation (SIRM) vs the ARM mean destructive field (MDFARM) of each sample, which is defined when the magnetic fraction loses half of its remanent magnetisation. It is indicative of the complicated relationship of mean grain size, where MDFARM increases with decrease in grain size. B) Leaf, exhaust and non-exhaust specimens are plotted on the Mrs/Ms versus ARM/Mrs for MD-SD (diamonds) and PSD-SD (circles) mixtures (Lascu et al., 2010). The numbers next to the symbols represent SD fraction in the total mixture.

Figure 8. FORC diagrams and their coercivity distribution as a function of log(field). (a-c) Brake pads show the coercivities on the higher end of the distribution spectrum while exhaust pipe specimens are on the lower end. Leaf specimens lie in between both, suggesting it has contribution from both endmembers. (D-G) FORC diagrams have been processed using VARIFORC smoothing (Harrison and Feinberg, 2008) using smoothing parameters SC,0= 10, Sb,0= 8, Sc,1= Sb, 1= 12, : 0.3. D) Average FORC of leaves showing presence of grains in vortex state, a low and high coercivity ridge E) brake pad sample has a distinctive vertical distribution along the Bu axis., indicative of presence MD grains sizes; FORC also shows a sharp SD tail extending to higher coercivity of 150-200 mT, suggestive of contribution from Fe-metal (see Fig. 4a) F) Rickshaw FORC shows a SD fingerprint with a PSD background. (G) XLI petrol exhaust shows interacting grains and an SP ridge. FORC= first-order reversal curve. FORC parameters used were: field step (H) = 1.5 mT, averaging time (t): 300 ms, T=300

Table 1A and B Room and low-temperature measurements for exhaust, non-exhaust, and leaf specimens. The contribution of superparamagnetic grains is given by $[\text{LT-SRIM}]_{10\text{K}}$ – $[\text{RT-SIRM}]_{10\text{K}}$/ [LT-SRIM]10K and loss of remanence from peak SIRM at room temperature is given by $[\text{RT-SIRM}]_{\text{MAX}}$- $[\text{RT-SIRM}]_{\text{MIN}}$/[$\text{RT-SIRM}]_{\text{MAX}}$

[Geochemistry, Geophysics, Geosystems]

Supporting Information for

Biomagnetic characterisation of air pollution particulates in Lahore, Pakistan

H.A. Sheikh[1], B.A. Maher[2], V., Karloukovski[2], G.I. Lampronti[1], R. J. Harrison[1]

[1]*Department of Earth Sciences, Downing Site, Cambridge, CB2 3EQ*

[2] *Centre for Environmental Magnetism and Palaeomagnetism, Lancaster Environment Centre, University of Lancaster, Lancaster, LA1 4YB, U.K.*

Contents of this file

Fig. S7 A) Hysteresis loops measured for specimens after subtracting the blank probe hysteresis measurement. N.B. weaker samples that were too noisy are excluded from this graph. B) Inset: showing the narrow opening of hysteresis loops.

Fig. S8 A) Hysteresis curves for brake pad and exhaust specimens. B) Inset: shows the coercivity of samples magnified at low field range.

Fig. S9 Coercivities of different specimens as measured from hysteresis

Fig. S10 Processed FORC diagram has been processed using VARIFORC smoothing (Harrison and Feinberg, 2008) using smoothing parameters T1_1Y_AW, T8_20d_AW, T6_1Y_AW, T10_1Y_TSL: smoothing parameters $S_{C,0}$= 8, $S_{b,0}$= 8, $S_{c,1}$= $S_{b,1}$= 16, λ : 0.2, output grid 2. Hyundai 2.6L Diesel Van exhaust $S_{C,0}$= 14, $S_{b,0}$= 12, $S_{c,1}$= $S_{b,1}$= 15, λ : 0.3, output grid 2. Mazda 3.5L exhaust: smoothing parameters $S_{C,0}$= 8, $S_{b,0}$= 8, $S_{c,1}$= $S_{b,1}$= 16, λ : 0.2, output grid 2 Rickshaw exhaust: smoothing parameters $S_{C,0}$= 8, $S_{b,0}$= 8, $S_{c,1}$= $S_{b,1}$= 16, λ : 0.2, output grid 2. XLI exhaust: smoothing parameters $S_{C,0}$= 5, $S_{b,0}$= 7, $S_{c,1}$= $S_{b,1}$= 12, λ : 0.3, output grid 2. Cultus Brake pad: smoothing parameters $S_{C,0}$= 6, $S_{b,0}$= 6, $S_{c,1}$= $S_{b,1}$= 10, λ : 0.2, output grid 2. Alto Brake pad: smoothing parameters $S_{C,0}$= 4, $S_{b,0}$= 4, $S_{c,1}$= $S_{b,1}$= 10, λ : 0.2, output grid 2. Mira Brake pad: smoothing parameters $S_{C,0}$= 12, $S_{b,0}$= 12, $S_{c,1}$= $S_{b,1}$= 20, λ : 0.2, output grid 3.

Fig. S11 XLI exhaust pipe specimen showing association of Fe-bearing particle with Mn

Fig. S12 XLI Exhaust pipe specimen shows the presence of heavy metals Cr and Al and Fe-bearing phase

Fig. S13 Diesel engines produce soot particles that are observed in the SEM. Ca is also associated with these particles

Fig. S14A Experimental (green curve), calculated (red curve) and difference (grey curve) patterns and peak positions (blue marks) from the Rietveld refinement of leaf sample T1_1Y_AW.

Fig. S14B Experimental (green curve), calculated (red curve) and difference (grey curve) patterns and Whewellite fit (blue) for sample T1_1Y_AW.

Fig. S14C Experimental (green curve), calculated (red curve) and difference (grey curve) patterns and Anhydrite fit (dark green)for sample T1_1Y_AW.

Fig. S14D Experimental (green curve), calculated (red curve) and difference (grey curve) patterns and anorthite (pink) fit for sample T1_1Y_AW.

Fig. S15 showing relationship of daily cumulative PM 2.5 with SIRM variation. Day 1 is assumed to have zero SIRM value. SIRM data points are Day 20 and Day 26. *PM 2.5 data are from US Consulate (open data source available at https://openaq.org/#/countries/PK)

Table S16 Brake pad and exhaust pipe vehicle specifications

Table S17 Summary of magnetic hysteresis data at room temperature (*N/A specimens were very noisy)

Table S18 Comparison of area-normalised SIRM from published magnetic studies

Table S19**.** shows a classification summary of different particles identified using the scanning electron microscope (SEM) and energy dispersive X-ray spectroscopy (EDX).

Introduction

Supporting information data file 1 for this manuscript includes additional morphological and chemical characterizations of leaf, exhaust-pipe residue and brake pad samples that were analyzed. Data were collected using a Quanta-650F scanning electron microscope equipped with an EDS detector. EDS spectra for regions of interests (either enumerated or individual analyses) are presented. Hysteresis data acquired from the AGM and additional processed first-order reversal curve (FORC) diagrams are also presented. Also given here are the XRD data for leaf specimens T10_1Y_TW and T10_20d_AW.

Supplementary data sets here include exhaust and non-exhaust vehicle specimens (S15), Magnetic hysteresis raw data from the AGM (S16), Comparison of normalized SIRM with previous studies (S17).

MPMS Sequence used for low temperature magnetic measurements is also included.

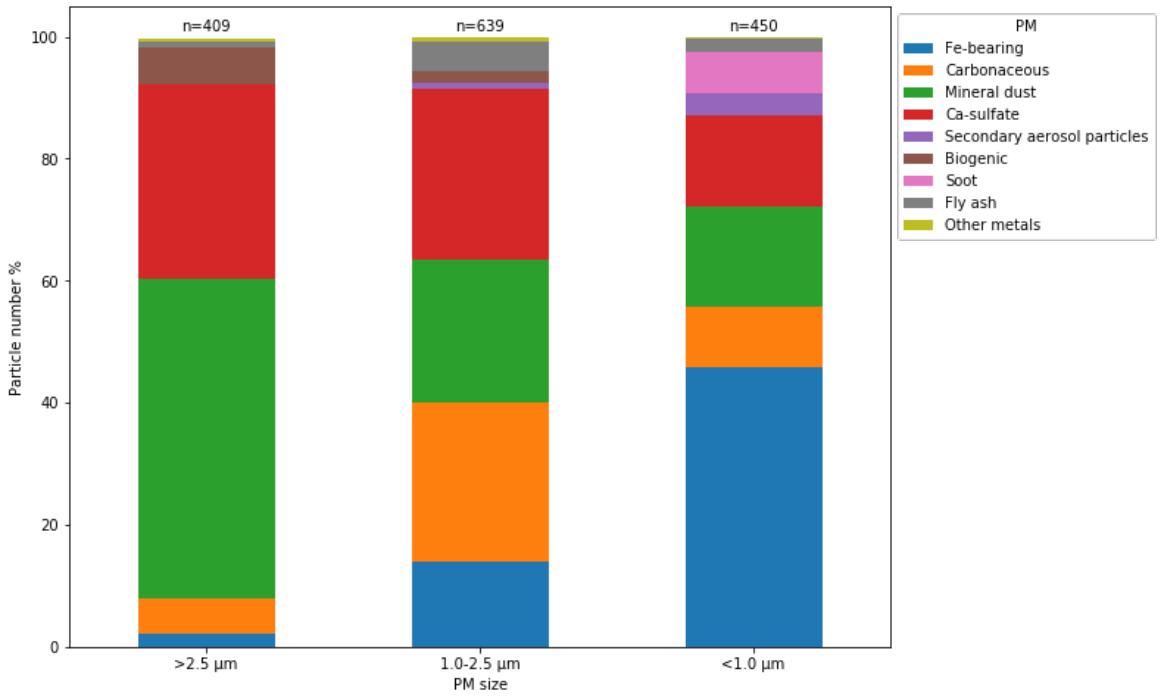

Figure S1. Particle number concentration based on BSE images and EDX maps. A total of 1482 particles was analysed and binned into three size ranges based on their largest axis diameter.

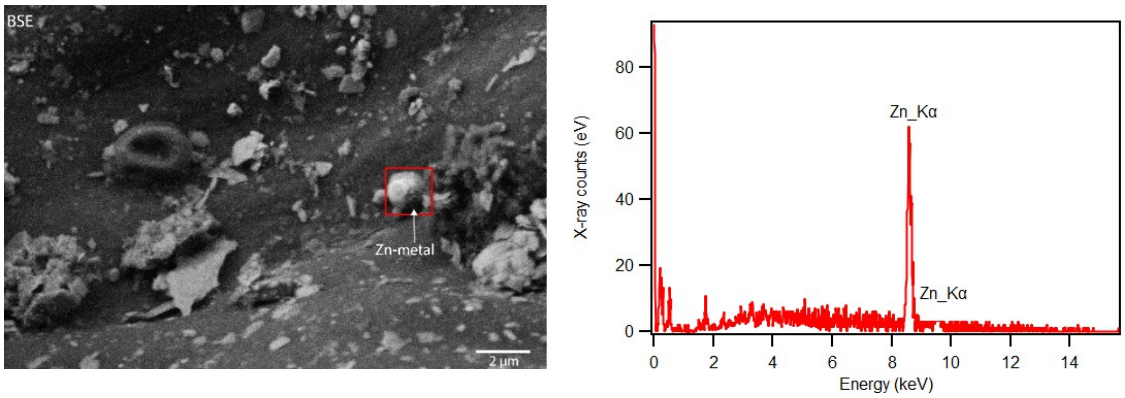

Figure S2. BSE image of a spherical Zn-metal particle and its EDX spectrum

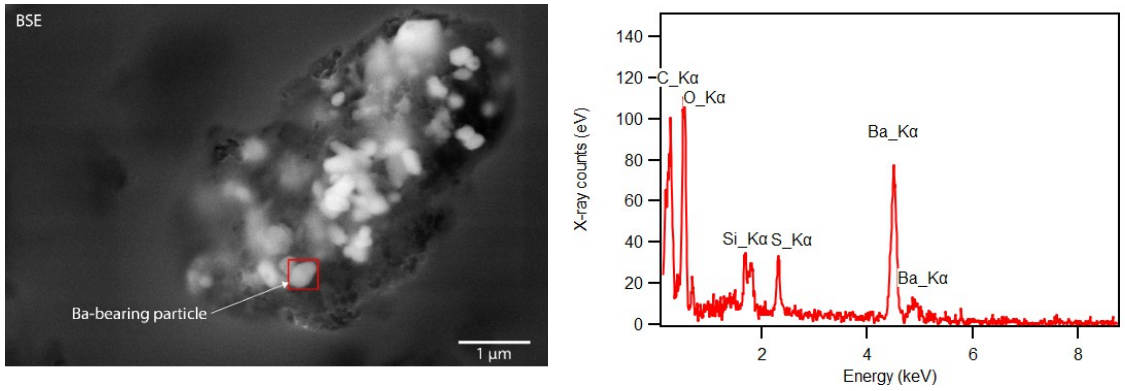

Figure S3. BSE image of a euhedral Ba-bearing particle around 0.5-1 µm and its corresponding EDX spectrum

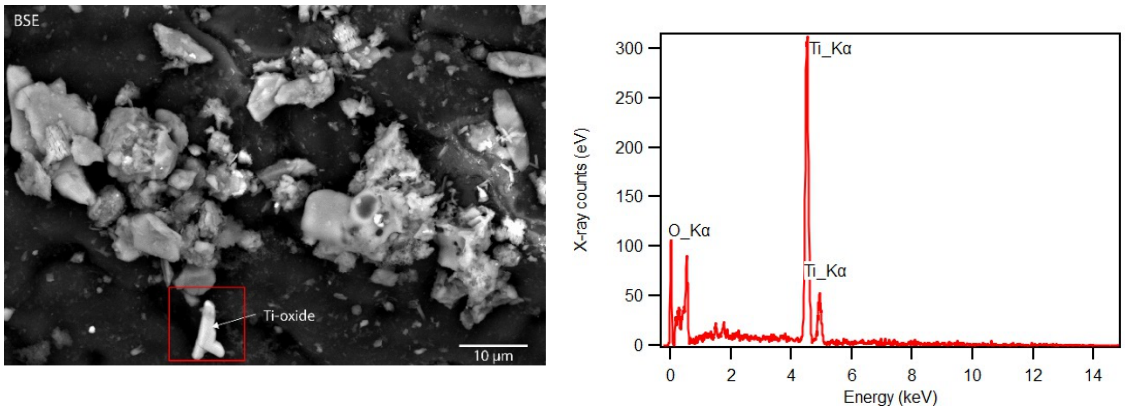

Figure S4. shows TiO_2 particle (~ 8 µm) and its corresponding EDX spectrum

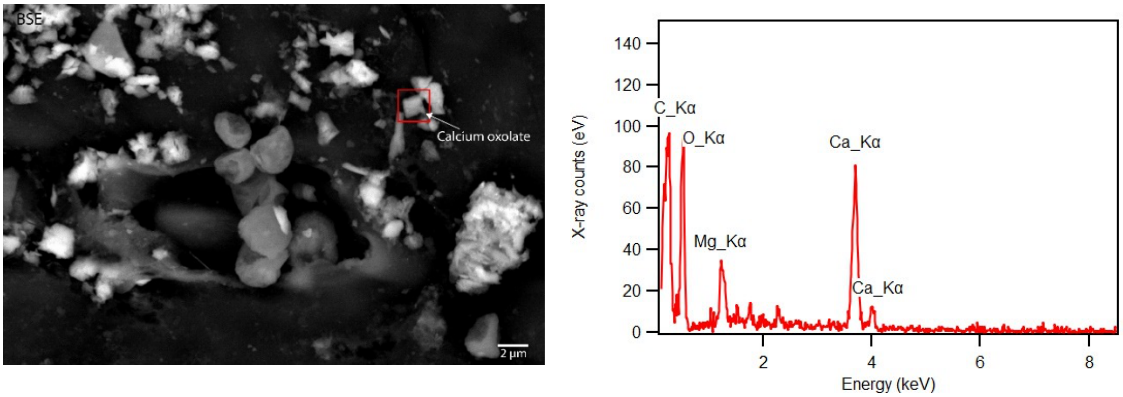

Figure S5. displays a rectangular calcium oxalate (whewellite) particle (~2 µm) (partly substituted by magnesium) and its corresponding EDX spectrum

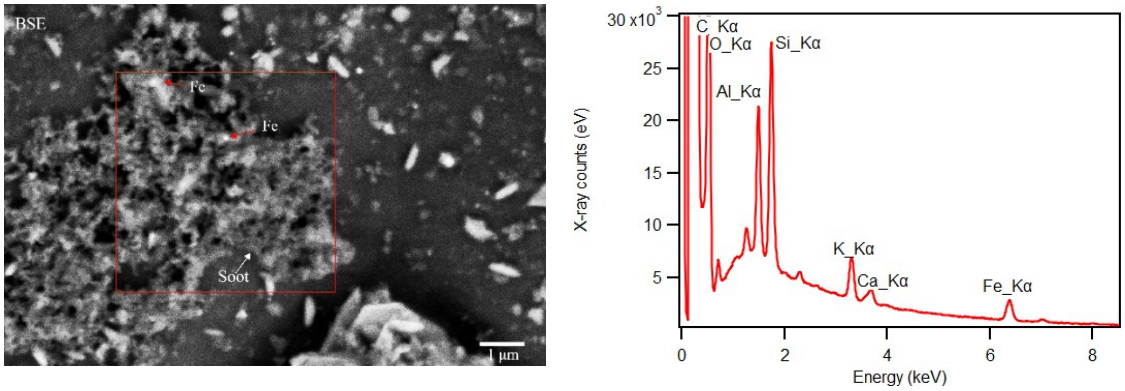

Figure S6. BSE image of nanoparticles of Fe embedded in soot and the corresponding EDX spectrum

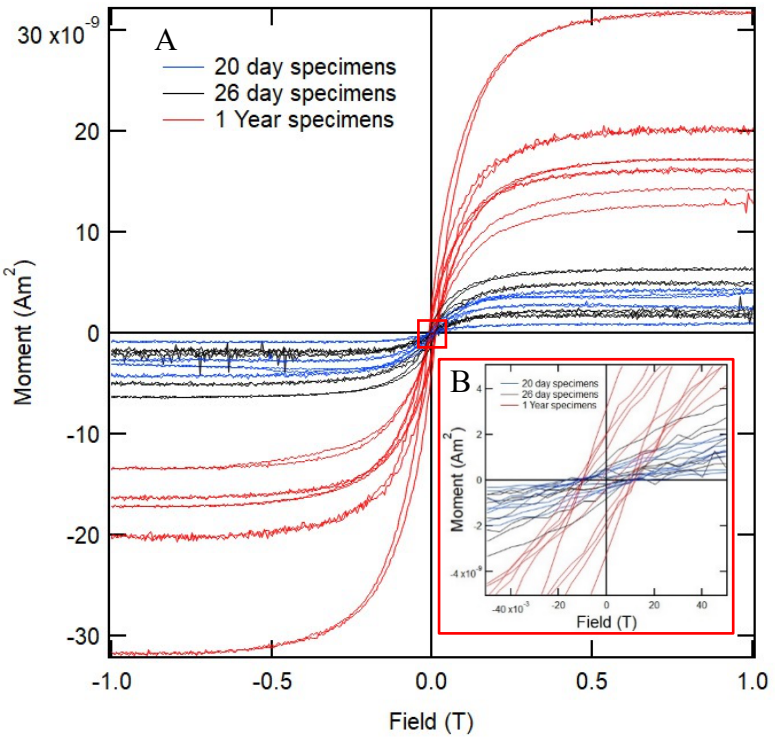

Figure S7. A) Hysteresis loops measured for specimens after subtracting the blank probe hysteresis measurement. N.B. weaker samples that were too noisy are excluded from this graph. B) Inset: showing the narrow opening of hysteresis loops.

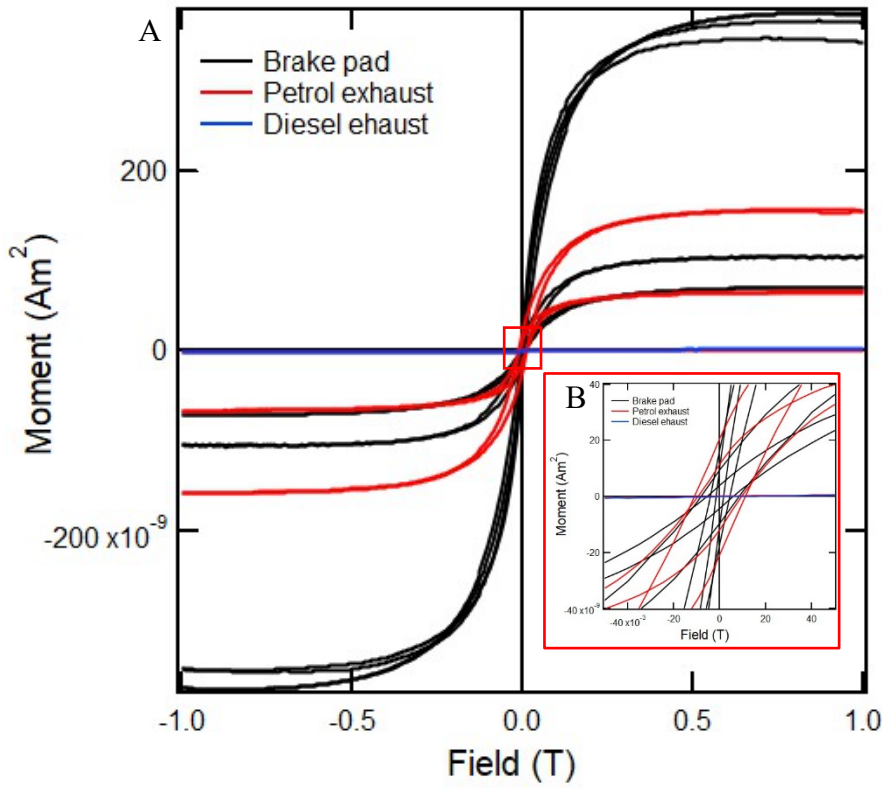

Figure S8. A) Hysteresis curves for brake pad and exhaust specimens. B) Inset: shows the coercivity of samples magnified at low field range.

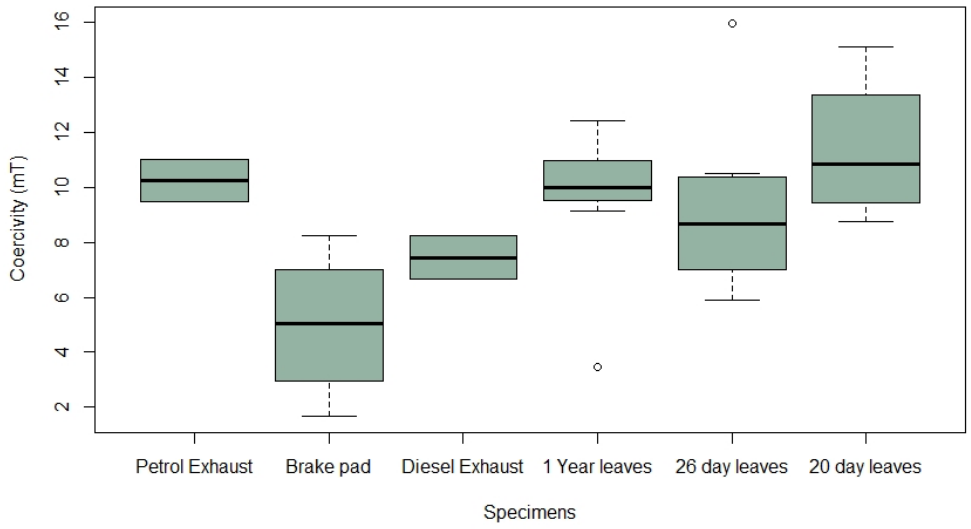

Figure S9. Coercivities of different specimens as measured from hysteresis

T10_1Y_TSL

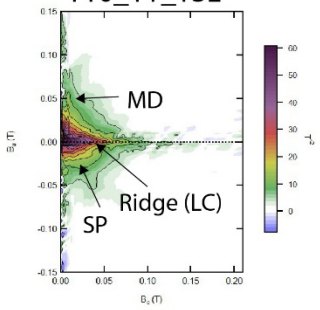

T6_1Y_AW

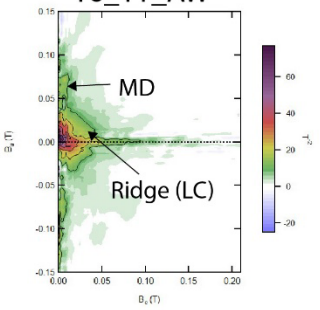

T1_1Y_AW

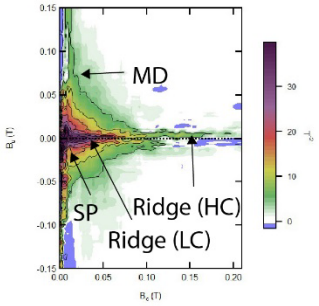

T2_6d_AW

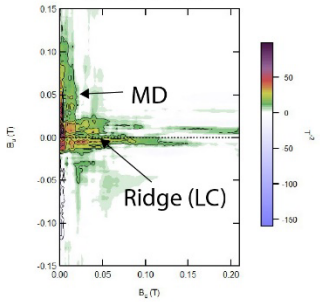

T8_20d_AW

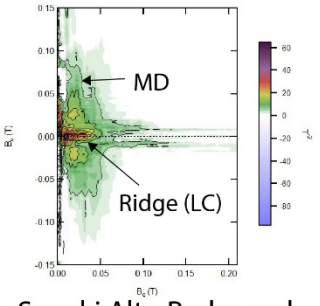

T7_20d_AW

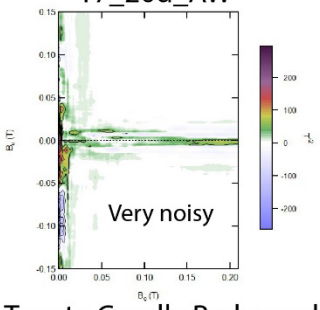

Toyota Mira Brake pad

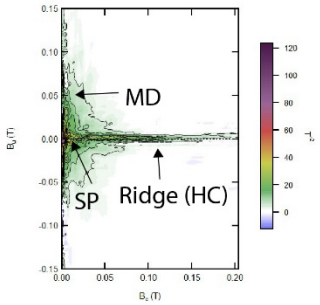

Suzuki Alto Brake pad

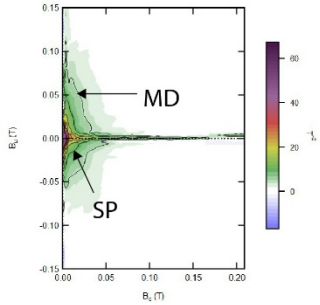

Toyota Corolla Brake pad

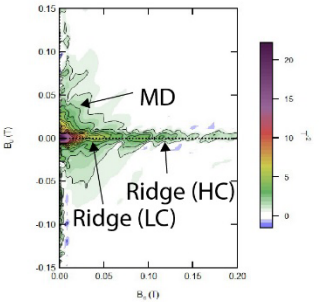

Suzuki Cultus Brake pad

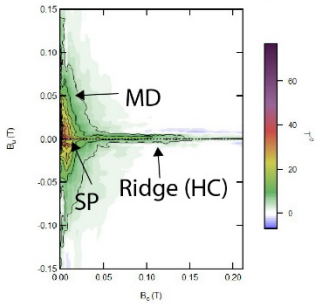

Toyota XLI Exhaust

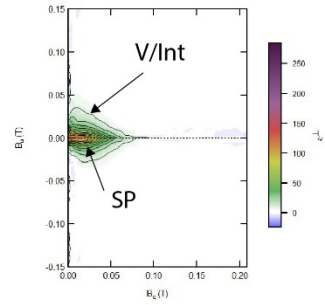

Rickshaw Exhaust

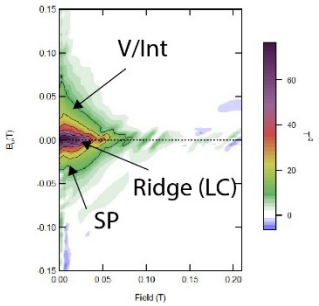

Hyundai 2.6 L Exhaust

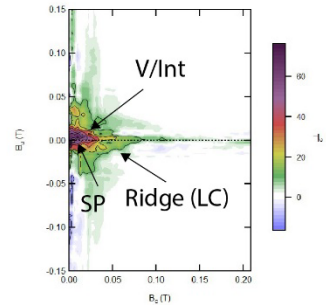

Mazda Truck 3.5L Exhaust

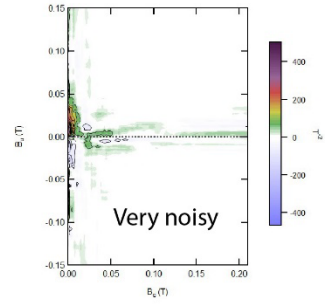

Figure S10. Processed FORC diagram has been processed using VARIFORC smoothing parameters (Harrison and Feinberg, 2008) T1_1Y_AW, T8_20d_AW, T6_1Y_AW, T10_1Y_TSL: smoothing parameters $S_{C,0}$= 8, $S_{b,0}$= 8, $S_{c,1}$= $S_{b,1}$= 16, λ : 0.2, output grid 2. Hyundai 2.6L Diesel Van exhaust $S_{C,0}$= 14, $S_{b,0}$= 12, $S_{c,1}$= $S_{b,1}$= 15, λ : 0.3, output grid 2. Mazda 3.5L exhaust: smoothing parameters $S_{C,0}$= 8, $S_{b,0}$= 8, $S_{c,1}$= $S_{b,1}$= 16, λ : 0.2, output grid 2 Rickshaw exhaust: smoothing parameters $S_{C,0}$= 8, $S_{b,0}$= 8, $S_{c,1}$= $S_{b,1}$= 16, λ : 0.2, output grid 2. XLI exhaust: smoothing parameters $S_{C,0}$= 5, $S_{b,0}$= 7, $S_{c,1}$= $S_{b,1}$= 12, λ : 0.3, output grid 2. Cultus Brake pad: smoothing parameters $S_{C,0}$= 6, $S_{b,0}$= 6, $S_{c,1}$= $S_{b,1}$= 10, λ : 0.2, output grid 2. Alto Brake pad: smoothing parameters $S_{C,0}$= 4, $S_{b,0}$= 4, $S_{c,1}$= $S_{b,1}$= 10, λ : 0.2, output grid 2. Mira Brake pad: smoothing parameters $S_{C,0}$= 12, $S_{b,0}$= 12, $S_{c,1}$= $S_{b,1}$= 20, λ : 0.2, output grid 3.

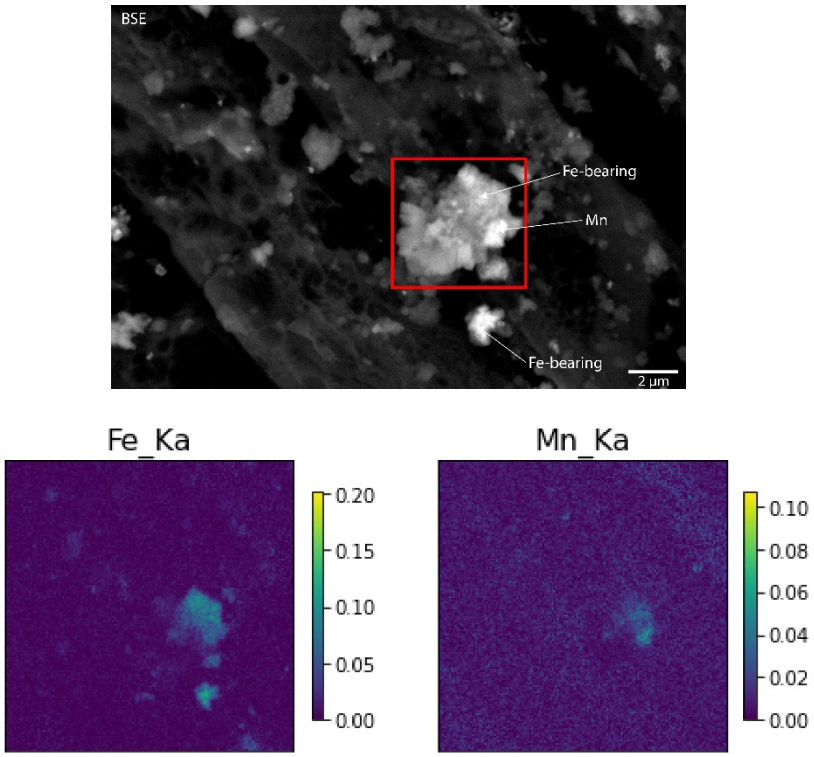

Figure S11. XLI exhaust pipe specimen showing association of Fe-bearing particle with Mn

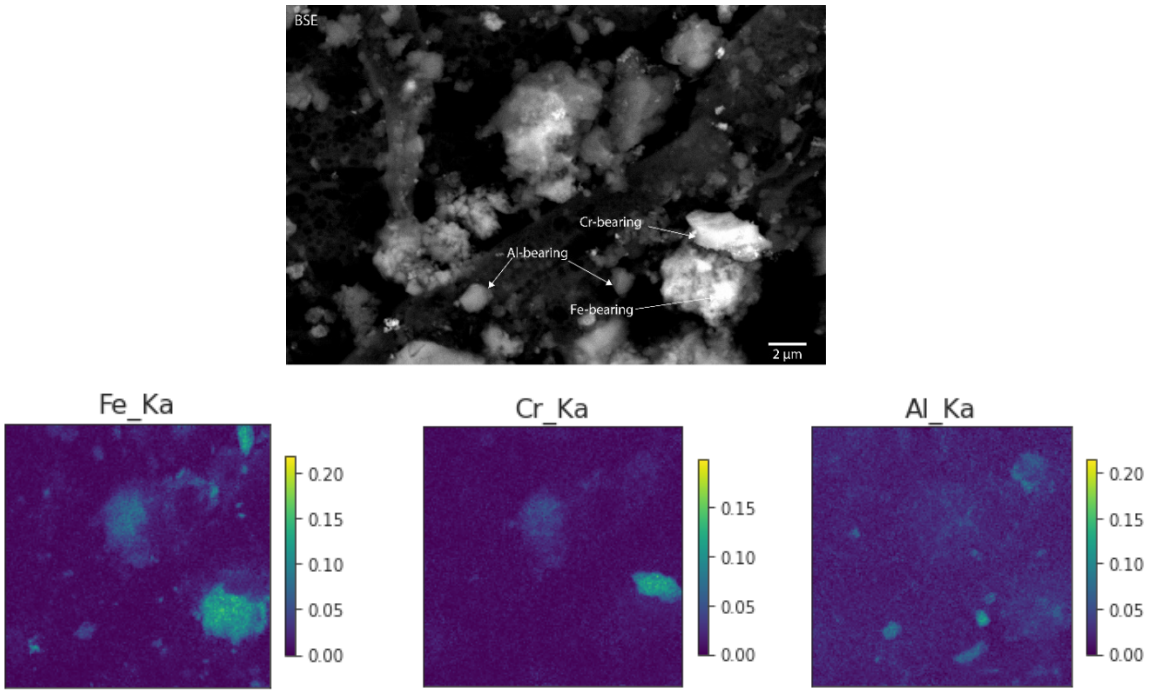

Figure S12. XLI Exhaust pipe specimen shows the presence of heavy metals Cr and Al and Fe-bearing phase

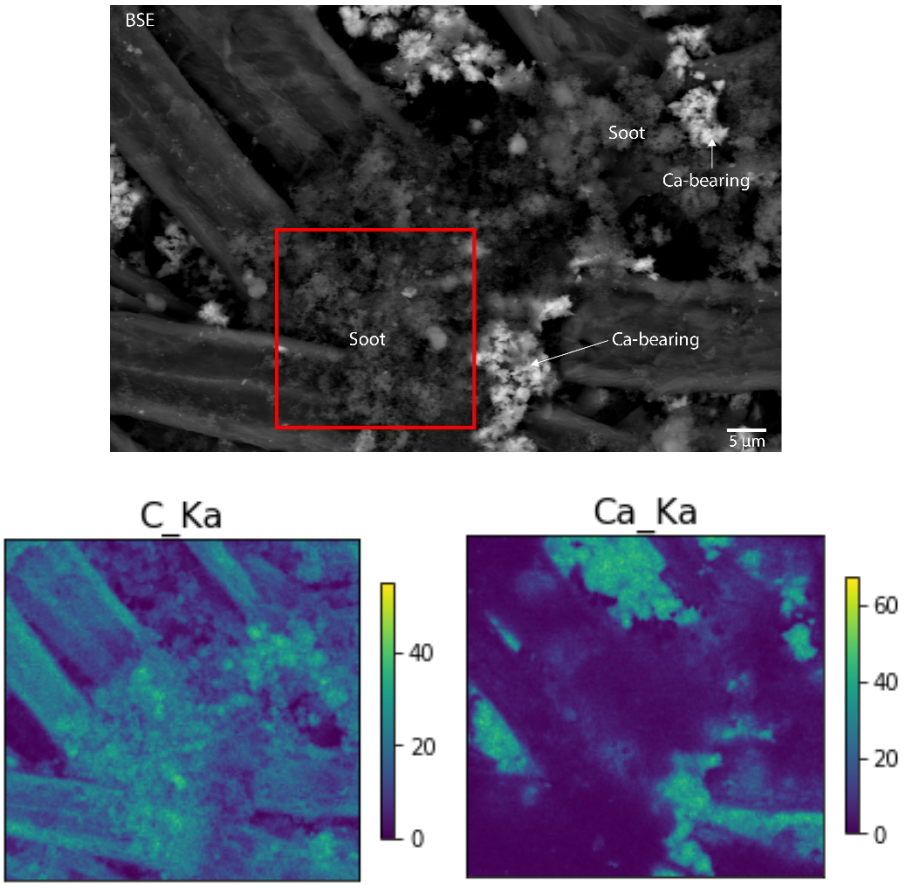

Figure S13. Diesel engines produce soot particles that are observed in the SEM. Ca is also associated with these particles

Powder XRD analyses of leaf sample T1_1Y_AW

Rietveld analysis was performed with the software Topas Academic V6 (Coelho, 2018). The structure of whewellite, anhydrite, and anorthite were retrieved from the Inorganic Crystal Structure Database (Hellenbrandt, 2004) No structural parameter other than unit cell parameters was refined. The March-Dollase model for preferred orientation (Dollase, 1986) was applied on the crystallographic planes parallel to (1 0 0) for whewellite and anhydrite. A shifted Chebyshev function with ten parameters was used to fit the background. The refinement converged with R_{wp} and X^2 equal to 2.44(%) and 2.53 respectively. Whewellite was found to be the dominant crystalline phase, 81(2) wt.%, then anorthite, 17(2) wt.%, and anhydrite, 2.8(0.6) wt.%. Rietveld refinement plot is reported in figure 8A.

Rietveld quantitative analysis is known to be unreliable for minor phases (<5 wt %). the accuracy is ± 1-2% relative for major phases, while the e.s.d. from the Rietveld calculation have no bearing on the accuracy or otherwise of the quantification itself, being merely related to the mathematical fit of the model (Madsen and Scarlett, 2008).

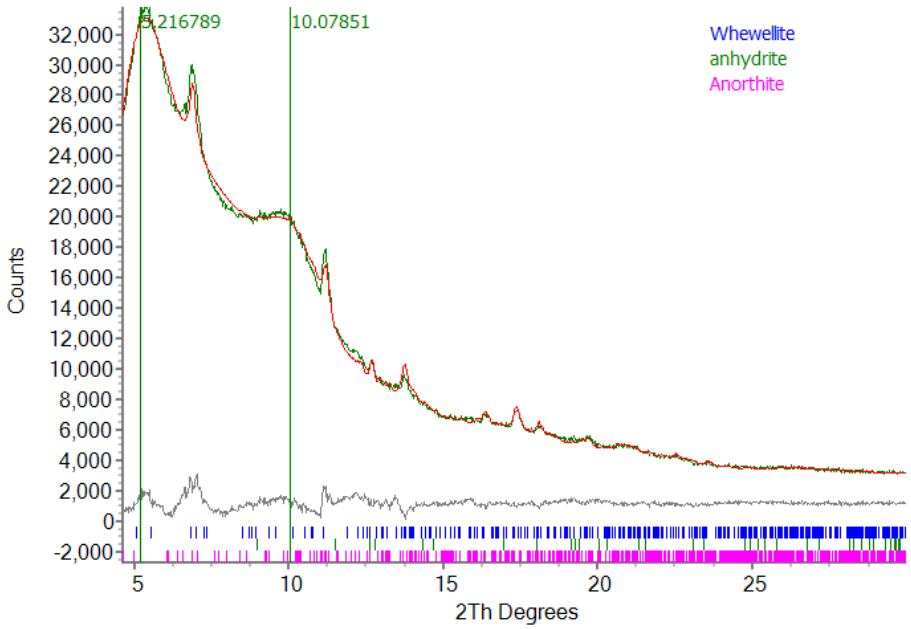

Figure S14A. Experimental (green curve), calculated (red curve) and difference (grey curve) patterns and peak positions (blue marks) from the Rietveld refinement of leaf sample T1_1Y_AW.

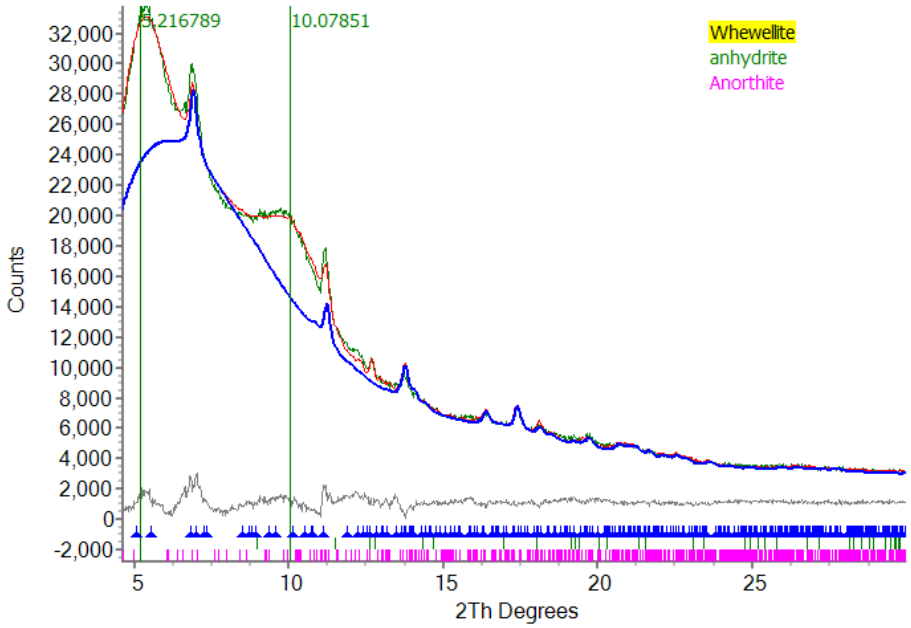

Figure S14B. Experimental (green curve), calculated (red curve) and difference (grey curve) patterns and Whewellite fit (blue) for sample T1_1Y_AW.

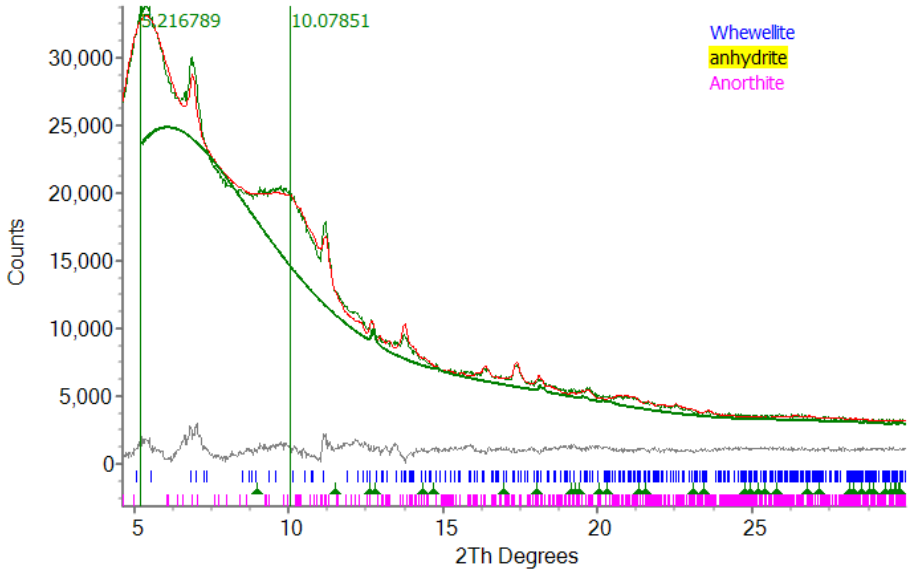

Figure S14C. Experimental (green curve), calculated (red curve) and difference (grey curve) patterns and Anhydrite fit (dark green) for sample T1_1Y_AW.

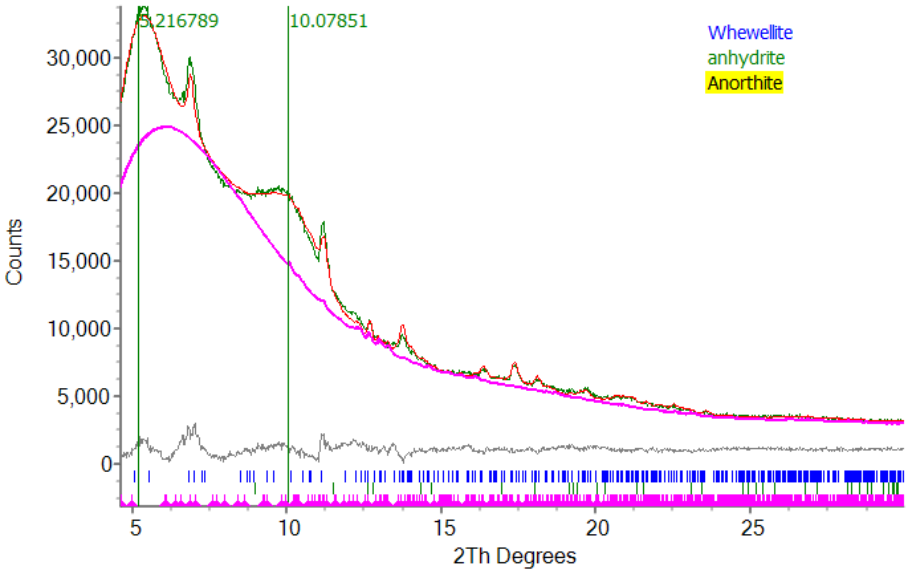

Figure S14D. Experimental (green curve), calculated (red curve) and difference (grey curve) patterns and anorthite (pink) fit for sample T1_1Y_AW.

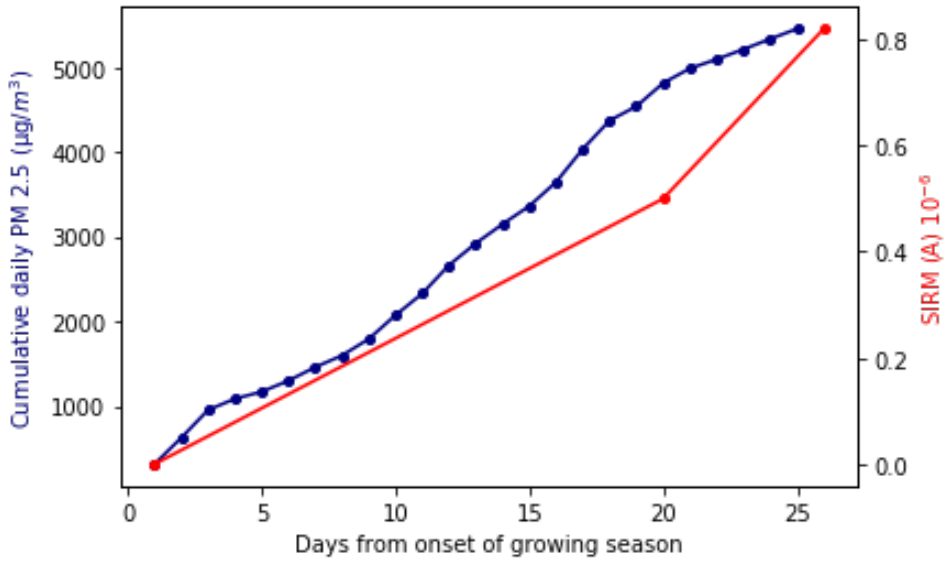

Figure S15. showing relationship of daily cumulative PM 2.5 with SIRM variation. Day 1 is assumed to have zero SIRM value. SIRM data points are Day 20 and Day 26. *PM 2.5 data are from US Consulate (open data source available at https://openaq.org/#/countries/PK)

Type	Make	Engine type	Engine Capacity (cc)
Brake pad	Toyota Corolla	Petrol	1300
	Toyota Mira	Petrol	660
	Suzuki Alto	Petrol	1000
	Suzuki Cultus	Petrol	1000
Exhaust Pipe	Mazda	Diesel	3500
	Hyundai	Diesel	2600
	Toyota XLI	Petrol	1300
	SA Rickshaw	Petrol and LNG	200

Table S16. Brake pad and exhaust pipe vehicle specifications

Specimen Name	*Specimen Type*	M_s (Am^2)	M_{rs} (Am^2)	B_c (mT)	B_{cr} (mT)	M_{rs}/M_s	B_{cr}/B_c
T1_1Y_AW	Leaf_01	1.71E-08	1.95E-09	12.40	45.50	1.14E-01	3.67E+00
T4_1Y_TW	Leaf_02	1.24E-08	1.08E-09	9.94	46.80	8.67E-02	4.71E+00
T1_20d_TW	Leaf_03	N/A	N/A	N/A	N/A	N/A	N/A
T1_6d_TW	Leaf_04	N/A	N/A	N/A	N/A	N/A	N/A
T2_6d_TW	Leaf_05	N/A	N/A	N/A	N/A	N/A	N/A
T2_6d_AW	Leaf_06	4.23E-09	5.30E-10	10.30	48.80	1.25E-01	4.76E+00
T3_6d_TW	Leaf_07	1.13E-08	1.06E-09	5.90	27.30	9.38E-02	4.63E+00
T4_6d_AW	Leaf_08	5.48E-09	5.77E-10	10.50	53.80	1.05E-01	5.12E+00
T5_1Y_AW	Leaf_09	1.43E-08	4.54E-10	3.48	202.27	3.18E-02	5.81E+01
T5_20d_AW	Leaf_10	N/A	N/A	N/A	N/A	N/A	N/A
T5_6d_TW	Leaf_11	N/A	N/A	N/A	N/A	N/A	N/A
T5_6d_AW	Leaf_12	N/A	N/A	N/A	N/A	N/A	N/A
T6_6d_TW	Leaf_13	N/A	N/A	N/A	N/A	N/A	N/A
T6_1Y_TW	Leaf_14	1.67E-08	1.45E-09	9.13	37.20	8.70E-02	4.08E+00
T6_20d_TW	Leaf_15	N/A	N/A	N/A	N/A	N/A	N/A
T6_6d_AW	Leaf_16	2.14E-09	3.32E-10	16.00	37.10	1.55E-01	2.32E+00
T7_1Y_TW	Leaf_17	2.06E-08	2.18E-09	10.90	35.31	1.06E-01	3.24E+00
T7_20d_TW	Leaf_18	2.61E-09	3.35E-10	11.60	61.93	1.29E-01	5.34E+00
T7_6d_AW	Leaf_19	N/A	N/A	N/A	N/A	N/A	N/A
T7_6d_TW	Leaf_20	4.23E-09	4.10E-10	7.89	32.30	9.68E-02	4.10E+00
T8_1Y_TW	Leaf_21	3.17E-08	3.21E-09	10.02	38.10	1.02E-01	3.80E+00
T8_20d_TW	Leaf_22	3.56E-09	3.84E-10	10.10	35.92	1.08E-01	3.56E+00
T8_6d_AW	Leaf_23	1.78E-09	1.42E-10	6.10	106.13	7.94E-02	1.74E+01
T8_6d_TW	Leaf_24	N/A	N/A	N/A	N/A	N/A	N/A
T9_20d_AW	Leaf_25	1.41E-09	2.00E-10	8.78	239.00	1.42E-01	2.72E+01
T9_20d_TW	Leaf_26	N/A	N/A	N/A	N/A	N/A	N/A
T10_20d_TSL	Leaf_27	8.71E-10	1.36E-10	15.10	31.90	1.56E-01	2.11E+00
T10_6d_ASL	Leaf_28	N/A	N/A	N/A	N/A	N/A	N/A
T10_6d_TSL	Leaf_29	6.34E-09	8.32E-10	8.68	30.32	1.31E-01	3.50E+00
T10_1Y_TSL	Leaf_30	1.90E-08	2.34E-09	11.1	36.74	1.23E-01	3.30E+00
Suzuki Alto	Brake Pad	3.74E-07	1.71E-08	4.26	44.15	4.57E-02	1.04E+01
Suzuki Cultus	Brake Pad	7.02E-08	4.15E-09	5.79	42.60	5.91E-02	7.36E+00
Toyota XLI	Brake Pad	3.59E-07	1.05E-08	1.67	43.20	2.92E-02	2.59E+01
Toyota Mira	Brake Pad	1.04E-07	9.46E-09	8.26	51.60	9.10E-02	6.25E+00
Mazda Truck 3.5L	Diesel Exhaust	1.47E-09	1.00E-10	6.68	93.5	6.80E-02	1.40E+01
Hyundai Van 2.6L	Diesel Exhaust	4.79E-09	5.72E-10	8.23	17.25	1.20E-01	2.09E+00
Super Asia Rickshaw	Petrol Exhaust	1.57E-07	2.09E-08	11.0	33.62	1.33E-01	3.05E+00
Toyota Corolla XLI	Petrol Exhaust	6.55E-08	1.17E-08	9.48	29.60	1.78E-01	3.12E+00

Table S17. Summary of magnetic hysteresis data at room temperature (*N/A specimens were very noisy)

Location	Study	Tree species	Leaf features	Average Leaf SIRM (A)	Days	Average PM 10 (ug/m3)
Lahore, Pakistan	This study	Bottlebrush	Hairy	2.33E-04	365	61
Lahore, Pakistan	This study	Bottlebrush	Hairy	2.42E-05	20	
Lahore, Pakistan	This study	Bottlebrush	Hairy	4.10E-05	26	
Antwerp, Belgium	Hofman et al. (2014)	Platanus × ac erifolia Willd.	Hairy	2.88E-05	157	22
Lancaster, UK	Mitchell and Maher (2009)	Tilia platyphyllos	Non-Hairy	8.10E-05	200	24
Ghent, Belgium	Kardel et al. (2011)	Carpinus betulus	Hairy (LPS)	8.50E-06	174	20
Ghent, Belgium	Kardel et al. (2011)	Carpinus betulus	Hairy (HPS)	4.20E-05	174	33
Ghent, Belgium	Kardel et al. (2011)	Carpinus betulus	Hairy (LPS)	1.75E-05	247	20
Ghent, Belgium	Kardel et al. (2011)	Carpinus betulus	Hairy (HPS)	8.50E-05	247	33
Ghent, Belgium	Kardel et al. (2011)	Tilia sp	Hairy (LPS)	1.55E-05	174	20
Ghent, Belgium	Kardel et al. (2011)	Tilia sp	Hairy (HPS)	5.20E-05	174	33
Ghent, Belgium	Kardel et al. (2011)	Tilia sp	Non-Hairy (LPS)	6.50E-06	174	20
Ghent, Belgium	Kardel et al. (2011)	Tilia sp	Non-Hairy (HPS)	2.05E-05	174	33
Ghent, Belgium	Kardel et al. (2011)	Tilia sp	Hairy (LPS)	3.05E-05	247	20
Ghent, Belgium	Kardel et al. (2011)	Tilia sp	Hairy (HPS)	9.40E-05	247	33
Ghent, Belgium	Kardel et al. (2011)	Tilia sp	Non-Hairy (LPS)	1.35E-05	247	20
Ghent, Belgium	Kardel et al. (2011)	Tilia sp	Non-Hairy (HPS)	4.20E-05	247	33

Table S18. comparison of area normalised SIRM from different magnetic studies

Particle type	*Mandatory elements*	*Other associated elements*	*Morphological features*	*Size-range (µm)*	*Potential sources*	*Nearest source in Lahore*
Fe-bearing	Fe	O, Zn, Cr, Al	Spherical or anhedral	<0.1-2.5	Industry, vehicular combustion	Industrial zones, Internal combustion engines, brake pad abrasion
Other metals		Zn, Ti, Mg, Mn, Cr, Al	Mostly spherical	1.0-2.5	Industrial, vehicular combustion, brake wear, tyre wear	Brake and tyre wear, vehicular engines, industrial estates
Fly Ash	Al, Si, O	Fe, Mn, Ca, Mg, K, F	Spherical	1.0 -2.5	Coal combustion (Shi et al., 2003)	Master power private or brick kilns outside Lahore
Soot	C	Fe	Chain-like spherical aggregates	0.1-0.2	Incomplete combustion or biomass burning (Buseck et al., 2014)	Mostly vehicular or increased biomass burning in winter
Carbonaceous	C	K, Cl, S	Spherical	0.1-2.5	Biomass burning, vehicular engine combustion	Carbon-rich particles, Tar from vehicular engine combustion
*Ca-sulfate**	Ca, O	C, S, Na, Mg	Elongated, needle-like, rectangular	0.5-2.5	Cement industry, construction	Plaster of Paris, construction of houses, limestone ($CaCO_3$)
Mineral dust	Si, Al, O	K, S, Ca, Fe, Na, Mg	Irregular shaped, both individual and complex aggregates	2.5-<10	Road dust, anthropogenic sources (Shi et al, 2003), crustal dust (non-anthropogenic)	Canal Road, nearby construction, nearest coal power plant, windblown during dust storms
K-rich	K, S, O	Cl, Ca, C	Subhedral-anhedral	K: 0.2-2.0	Biomass burning and diesel engine combustion	Biomass burning of Kharif crop in Pakistan and India, coal power plants, engine combustion, nearby brick kilns
Biogenic	C		Spherical	1.0-7.5	Pollen	Flowers, plants

Table S19. shows a classification summary of different particles identified using the scanning electron microscope (SEM) and energy dispersive X-ray spectroscopy (EDX).

MPMS Sequence

New Datafile "C:\QdSquidVsm\Data\Hassan has57\020721_T10-1y-tsl_further_tests\020721_T10-1y-tsl_further_tests_1_RT_remanence.dat"
Set Magnetic Field 25000.0Oe at 500.00Oe/sec, Linear, Stable
Wait For Temperature, Field, Delay 300 secs (5.0 mins), No Action
Set Magnetic Field 0.0Oe at 500.00Oe/sec, No O'Shoot, Stable
Wait For Temperature, Field, Delay 300 secs (5.0 mins), No Action
Magnet Reset
Wait For Temperature, Field, Delay 1200 secs (20.0 mins), No Action
DC Measure 10 scans over 35 mm in 4 sec Auto-Tracking
Wait For Temperature, Field, Delay 60 secs (1.0 mins), No Action

New Datafile "C:\QdSquidVsm\Data\Hassan has57\020721_T10-1y-tsl_further_tests\020721_T10-1y-tsl_further_tests_2_RT-SIRM_cooldown_in_ZF.dat"
MPMS3 Moment (DC) vs Temperature 300K to 10K Sweep Continuous Auto-Tracking
Wait For Temperature, Field, Delay 60 secs (1.0 mins), No Action

New Datafile "C:\QdSquidVsm\Data\Hassan has57\020721_T10-1y-tsl_further_tests\020721_T10-1y-tsl_further_tests_3_RT-SIRM_warm_up_in_ZF.dat"
MPMS3 Moment (DC) vs Temperature 10K to 300K Sweep Continuous Auto-Tracking
Wait For Temperature, Field, Delay 60 secs (1.0 mins), No Action

Set Temperature 10K at 35K/min. Fast Settle
Wait For Temperature, Field, Delay 600 secs (10.0 mins), No Action

New Datafile "C:\QdSquidVsm\Data\Hassan has57\020721_T10-1y-tsl_further_tests\020721_T10-1y-tsl_further_tests_4_10K_remanence.dat"
Set Magnetic Field 25000.0Oe at 500.00Oe/sec, Linear, Stable
Wait For Temperature, Field, Delay 300 secs (5.0 mins), No Action
Set Magnetic Field 0.0Oe at 500.00Oe/sec, No O'Shoot, Stable
Wait For Temperature, Field, Delay 300 secs (5.0 mins), No Action
Magnet Reset
Wait For Temperature, Field, Delay 1200 secs (20.0 mins), No Action
DC Measure 10 scans over 35 mm in 4 sec Auto-Tracking
Wait For Temperature, Field, Delay 60 secs (1.0 mins), No Action

New Datafile "C:\QdSquidVsm\Data\Hassan has57\020721_T10-1y-tsl_further_tests\020721_T10-1y-tsl_further_tests_5_LT-SIRM_warm_up_in_ZF.dat"
MPMS3 Moment (DC) vs Temperature 10K to 300K Sweep Continuous Auto-Tracking
Wait For Temperature, Field, Delay 60 secs (1.0 mins), No Action

Set Magnetic Field 25000.0Oe at 500.00Oe/sec, No O'Shoot, Stable
Wait For Temperature, Field, Delay 600 secs (10.0 mins), No Action

New Datafile "C:\QdSquidVsm\Data\Hassan has57\020721_T10-1y-tsl_further_tests\020721_T10-1y-tsl_further_tests_6_MvT_cooldown_in_25000Oe.dat"
MPMS3 Moment (DC) vs Temperature 300K to 10K Sweep Continuous Auto-Tracking

Wait For Temperature, Field, Delay 60 secs (1.0 mins), No Action

New Datafile "C:\QdSquidVsm\Data\Hassan has57\020721_T10-1y-tsl_further_tests\020721_T10-1y-tsl_further_tests_7_10K_remanence_after_FC.dat"
Set Magnetic Field 0.0Oe at 500.00Oe/sec, No O'Shoot, Stable
Wait For Temperature, Field, Delay 300 secs (5.0 mins), No Action
Magnet Reset
Wait For Temperature, Field, Delay 1200 secs (20.0 mins), No Action
DC Measure 10 scans over 35 mm in 4 sec Auto-Tracking
Wait For Temperature, Field, Delay 60 secs (1.0 mins), No Action

New Datafile "C:\QdSquidVsm\Data\Hassan has57\020721_T10-1y-tsl_further_tests\020721_T10-1y-tsl_further_tests_8_LT-SIRM_warm_up_in_ZF_after_FC.dat"
MPMS3 Moment (DC) vs Temperature 10K to 300K Sweep Continuous Auto-Tracking
Wait For Temperature, Field, Delay 60 secs (1.0 mins), No Action